Atmos. Meas. Tech., 10, 4209–4234, 2017
https://doi.org/10.5194/amt-10-4209-2017

Atmospheric Measurement Techniques
Open Access
EGU

The novel HALO mini-DOAS instrument: inferring trace gas concentrations from airborne UV/visible limb spectroscopy under all skies using the scaling method

Tilman Hüneke[1], Oliver-Alex Aderhold[1], Jannik Bounin[1], Marcel Dorf[1,a], Eric Gentry[1,b], Katja Grossmann[1,c], Jens-Uwe Grooß[2], Peter Hoor[3], Patrick Jöckel[4], Mareike Kenntner[1,d], Marvin Knapp[1], Matthias Knecht[1], Dominique Lörks[1], Sabrina Ludmann[1,e], Sigrun Matthes[4], Rasmus Raecke[1], Marcel Reichert[1], Jannis Weimar[1,f], Bodo Werner[1], Andreas Zahn[5], Helmut Ziereis[4], and Klaus Pfeilsticker[1]

[1]Institut für Umweltphysik, University of Heidelberg, Heidelberg, Germany
[2]Forschungszentrum Jülich, Institute of Energy and Climate Research – Stratosphere (IEK-7), Jülich, Germany
[3]Institut für Physik der Atmosphäre, University of Mainz, Mainz, Germany
[4]Deutsches Zentrum für Luft- und Raumfahrt, Institut für die Physik der Atmosphäre, Oberpfaffenhofen, Germany
[5]Karlsruhe Institute of Technology (KIT), Institute for Meteorology and Climate Research, Karlsruhe, Germany
[a]now at: Max-Planck-Institute for Chemistry, Mainz, Germany
[b]now at: Department of Astronomy and Astrophysics, University of California Santa Cruz, Santa Cruz, California, USA
[c]now at: Joint Institute For Regional Earth System Science and Engineering (JIFRESSE), University of California Los Angeles, Los Angeles, California, USA
[d]now at: Deutsches Zentrum für Luft- und Raumfahrt, Institut für die Physik der Atmosphäre, Oberpfaffenhofen, Germany
[e]now at: IFEU – Institut für Energie- und Umweltforschung Heidelberg GmbH, Heidelberg, Germany
[f]now at: Physikalisches Institut, University of Heidelberg, Heidelberg, Germany

Correspondence to: Tilman Hüneke (tilman.hueneke@iup.uni-heidelberg.de)

Received: 30 March 2017 – Discussion started: 27 April 2017
Revised: 19 September 2017 – Accepted: 24 September 2017 – Published: 8 November 2017

Abstract. We report on a novel six-channel optical spectrometer (further on called mini-DOAS instrument) for airborne nadir and limb measurements of atmospheric trace gases, liquid and solid water, and spectral radiances in the UV/vis and NIR spectral ranges. The spectrometer was developed for measurements from aboard the German High-Altitude and Long-Range (HALO) research aircraft during dedicated research missions. Here we report on the relevant instrumental details and the novel scaling method used to infer the mixing ratios of UV/vis absorbing trace gases from their absorption measured in limb geometry. The uncertainties of the scaling method are assessed in more detail than before for sample measurements of NO_2 and BrO. Some first results are reported along with complementary measurements and comparisons with model predictions for a selected HALO research flight from Cape Town to Antarctica, which was performed during the research mission ESMVal on 13 September 2012.

1 Introduction

In the past 3 decades airborne UV/vis spectroscopy measurements developed into a powerful tool to study the photochemistry and radiative properties of the atmosphere. The approach is based on the pioneering work of Noxon (1975) and later Noxon et al. (1979) to exploit ground-based spectroscopic observations of the zenith-scattered skylight to monitor stratospheric NO_2 (and later O_3, BrO, and OClO, see below). The technique was further improved after the discovery of the ozone hole in 1985. Within the framework of ozone hole research, zenith sky UV/vis measurements were performed not only from the ground (e.g. Solomon et al., 1987a) but also from research aircrafts. Optical spectrometers were deployed on the NASA DC-8 during Airborne Arctic Stratospheric Expedition (AASE) in 1989 (e.g. Wahner et al., 1990a, b; Schiller et al., 1990) and later (1992–1995) on the German Transall (e.g. Brandtjen et al., 1994;

Pfeilsticker and Platt, 1994). The spectroscopic analysis of the measured skylight spectra for the detection of O_3, NO_2, BrO, and OClO was based on differential optical absorption spectroscopy (DOAS) (for a recent overview see Platt and Stutz, 2008), and assisting radiative transfer (RT) calculations allowed the estimation of the integrated overhead (or total) column density of the targeted gases (Solomon et al., 1987b).

McElroy et al. (1999) were the first to exploit airborne nadir-scattered skylight measurements to study plumes of BrO in the lower troposphere during Arctic spring. Later airborne multi-axis DOAS measurements by Bruns et al. (2004, 2006) over Europe and on major air traffic corridors by Dix et al. (2009) within the CARIBIC project (http://www.caribic-atmospheric.com/) were used to gain information on the distribution and photochemistry of pollutants and their products within the troposphere (e.g. Heue et al., 2014).

Meanwhile, more versatile DOAS-based 2-D imaging nadir techniques have become available to monitor the ground for sources and sinks of UV/visible/NIR absorbing radicals, pollutants and their products, and greenhouse gases (e.g. Heue et al., 2008; Gerilowski et al., 2011; Beirle et al., 2011; Merlaud et al., 2012; General et al., 2014).

Airborne UV/vis measurements in limb geometry started with the balloon-borne study of Weidner et al. (2005), which aimed at studies of the photochemistry, budgets, and variation of the NO_x (Kritten et al., 2010, 2014) and BrO_x (Kreycy et al., 2013) families in the stratosphere. The airborne limb measurements of scattered skylight continued with the aircraft studies of Prados-Roman et al. (2011) made from aboard the DLR Falcon and more recently from the American High-performance Instrumented Airborne Platform for Environmental Research (HIAPER) aircraft (Volkamer et al., 2015), the NSF/NCAR C-130 (Gratz et al., 2015; Ye et al., 2016), the NASA Global Hawk (Stutz et al., 2017; Werner et al., 2017), and those reported here from HALO, an aircraft based on a Gulfstream G550 jet (http://www.halo.dlr.de/). For first results from measurement campaigns involving the HALO mini-DOAS instrument, the reader is referred to e.g. Wendisch et al. (2016), Voigt et al. (2017), Wolf et al. (2017), and Jurkat et al. (2017). Table 1 lists all deployments of the HALO mini-DOAS instrument in recent years.

One common facet of all these airborne UV/vis limb measurements is the need for a stable observation geometry (or pointing) of the telescopes (required are a few tenths of a degree), in order to render the underlying mathematical inversion problem for trace gas retrievals meaningful (Rodgers, 2000). Therefore, all modern airborne UV/vis spectrometers collect skylight from actively controlled telescopes to compensate for the movements (i.e. the roll and pitch angle) of the airborne measurement platform. Most conveniently the attitude data to control the telescope's pointing are provided by the aircraft's inertial navigation system or by custom-built attitude systems (e.g. Baidar et al., 2013).

Airborne DOAS limb measurements however come with two major difficulties.

The first results from the necessity to know the amount of absorption of the targeted species in the background spectrum. In skylight DOAS all measurements are referred to a background spectrum recorded with the same instrument, since the measured atmospheric absorptions are much smaller (optical densities of atmospheric absorbers typically range between 10^{-4} and 10^{-2}) than those due to the Fraunhofer lines of the sun's photosphere. Different strategies are available to determine the absorption in the background spectrum, depending on the available observation geometries and target gas. Most easy to deal with are gases with little or negligible amounts located overhead the aircraft (e.g. CH_2O, $C_2H_2O_2$, HONO, often IO, OClO at daytime) because their absorption in the background spectrum is then small or even negligible. It is far more complicated to determine the amount of absorption in the background spectrum of gases with considerable (and often spatially and temporally varying) amounts located overhead the aircraft (e.g. O_3, O_4, NO_2, BrO). Here, direct sun or zenith sky observations are helpful (e.g. Volkamer et al., 2015; Stutz et al., 2017), but for fast-moving aircrafts the overhead column density may change too rapidly to carry out Langley-type regressions of the measured absorption as a function of air mass (see Gurlit et al., 2005; Dorf et al., 2008). Therefore, the amount of absorption in the background spectrum and its contribution to the total absorption needs to be minimised (e.g. by referring all measurements to low solar zenith angle observations at high altitude) such that the remaining absorption eventually can be calculated using model predictions (see below).

The second major difficulty comes from the necessity to constrain the RT in the atmosphere. The latter is needed for the interpretation of UV/vis limb measurements when assigning concentrations to the different locations in the atmosphere, which is often carried out using inversion techniques such as optimal estimation (Rodgers, 2000). Unfortunately, in a heavily aerosol-loaded or even cloudy atmosphere, light paths (or light path distributions) are not well-defined due to multiple scattering of collected skylight. Therefore, the inversion problem becomes almost intractable when the RT forward model is not constrained by means other than the aircraft and telescope attitude, celestial geometry of the sun and earth, and atmospheric pressure and temperature data. Additional data on the micro-physical properties and spatial distribution of aerosols and cloud particles are required. These are often taken from in situ aerosol measurements, lidar or radar observations, model predictions of the spatial distribution of the measured gases, observations or predictions of the cloud cover, etc. Because these parameters are usually not known sufficiently well for applications with fast-moving aircraft platforms, the employed retrieval strategies often rely on constraining the RT by the slant column density of simultaneously measured absorption bands of the collisional complex O_2-O_2 (in the following briefly called O_4) and/or rela-

Table 1. Science mission deployments of the HALO mini-DOAS instrument from 2012 to 2016.

Date	Name		Flights	Hours	References
Aug–Sep 2012	TACTS/ESMVal	Transport and Composition in the UT/LS/Earth System Model Validation	11	112	Jurkat et al. (2014, 2017); Vogel et al. (2014); Rolf et al. (2015); Müller et al. (2016)
Dec–Jan 2013/14	NARVAL	Next Generation Remote Sensing for Validation Studies	15	120	Klepp et al. (2014)
Mar–Apr 2014	ML-Cirrus	Mid-Latitude Cirrus	16	77	Voigt et al. (2017); Wolf et al. (2017)
Aug–Oct 2014	ACRIDICON	Aerosol, Cloud, Precipitation, and Radiation Interactions and Dynamics of Convective Cloud Systems	14	96	Wendisch et al. (2016)
Jul–Aug 2015	OMO	Oxidation Mechanism Observations	20	116	
Dec–Mar 2015/16	POLSTRACC	Polar Stratosphere in a Changing Climate	18	156	

tive radiances (e.g. Bruns et al., 2006; Prados-Roman et al., 2011; Baidar et al., 2013).

For airborne applications, constraining the RT by O_4 comes with some limitations. First of all, the absorption of O_4 is $\propto [O_2]^2$, and thus skylight is much more efficiently absorbed in the lower parts of the troposphere than in the upper troposphere or stratosphere. A (a priori unknown) fraction of the UV/vis light collected in limb geometry measurements in the middle and upper troposphere or lower stratosphere may be backscattered from lower parts of the atmosphere (Oikarinen, 2002). A changing ground albedo or cloud cover at low levels may thus modulate the measured limb slant column density of O_4 higher up in the atmosphere. Therefore, changing scattering properties of the troposphere – even of those parts which are not being directly sampled by the telescope's field of view (FOV) – may mimic the presence (or absence) of aerosols and cloud particles at flight altitude (Stutz et al., 2017). If a significant fraction of the targeted gas is located off the telescope's FOV, assigning proper amounts of the measured gas to the correct locations in the atmosphere thus becomes ambiguous or even impossible. In consequence, until the recent past, the retrievals of UV/vis limb measurements had been restricted to clear or almost clear sky observations.

In order to render the interpretation of airborne UV/vis limb measurements more tractable for all kind of skies, in particular for measurements in partly cloudy skies, we recently developed the so-called scaling method (Raecke, 2013; Großmann, 2014; Werner, 2015; Hüneke, 2016; Stutz et al., 2017; Werner et al., 2017). The scaling method makes use of the concentration of a scaling gas, either in situ measured (e.g. O_3) or calculated (e.g. O_4), which is used together with the slant column densities from simultaneously measured spectra of the scaling gas (further on denoted P) and the targeted gases (further on denoted X), preferentially monitored in the same wavelength region. The latter appears to be advantageous in order to minimise any wavelength dependence of the atmospheric Rayleigh and Mie scattering (see Stutz et al., 2017, and its supplement, and below). The in situ measured concentration and the remotely observed absorption of the scaling gas P can then be used to infer an effective light path length (or distribution) common for the gases P and X (see Sect. 3 below). The underlying assumption is a horizontally constant trace gas concentration along the line of sight equal to the in situ measured concentration. One draw-back of the scaling method comes from its (moderate) sensitivity towards the relative vertical profile shapes (but not absolute concentrations) of the involved trace gases. The sensitivity can best be dealt with by using a scaling gas P with a similar profile shape to that of the target gas X. The relative profile shapes of both gases can then be taken from either in situ measurements performed during dives of the aerial vehicle, any a priori knowledge, and/or from chemistry transport models (CTMs, e.g. CLaMS, SLIMCAT) or chemistry climate models (CCMs, e.g. EMAC; for information on the models see Sect. 3.5). Incorporating model predictions is very straightforward since the limb measurements are often used to validate the framework of predictions together with the other complementary measurements performed on board the respective research aircrafts.

The present study describes the novel UV/vis/NIR HALO mini-DOAS instrument and explores the scaling method in more detail together with its uncertainties and potential errors.

The paper is structured as follows. In Sect. 2 the instrument is described and characterized. Details of the employed

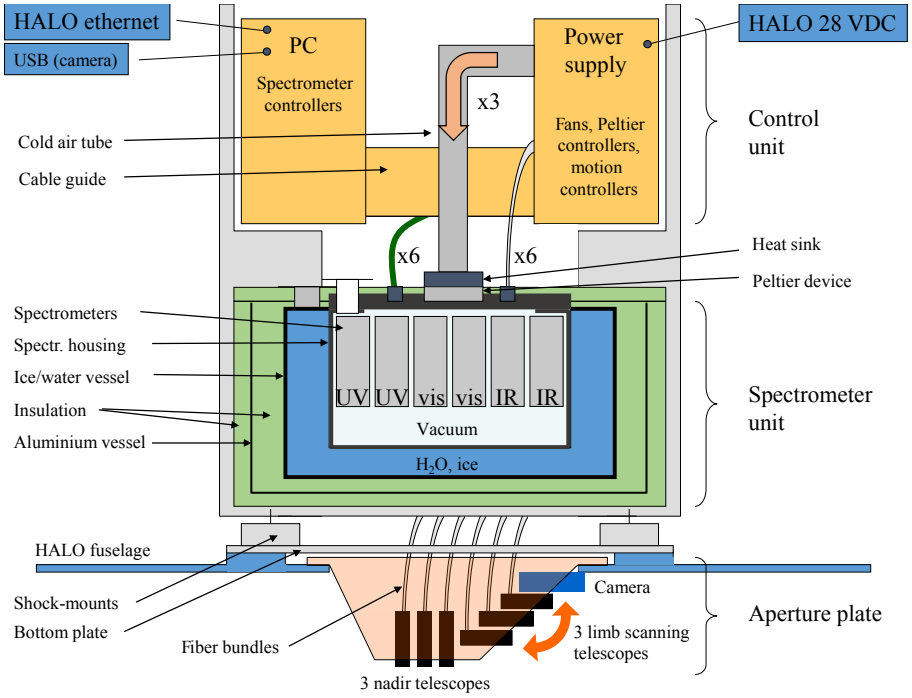

Figure 1. Sketch of the HALO mini-DOAS instrument.

methods are provided in Sect. 3. These include the spectral retrieval, RT calculation, complementary measurements, CTM and CCM modelling, and a description of the scaling method and its uncertainties. Section 4 describes sensitivity studies of the retrieval method by comparing inferred [NO_2] using different CTM and CCM trace gas profile predictions and different scaling gases. Finally, our results for inferred [NO_2] and [BrO] are intercompared with complementary measurements and model predictions for a HALO flight from Cape Town to Antarctica during austral spring 2012 (Sect. 5). Section 6 concludes the study.

2 Instrument description

The novel mini-DOAS instrument builds on the heritage of similar instruments assembled by our research group and collaborating partners for deployments on aircraft (e.g. the DLR Falcon, Geophysica, NASA Global Hawk, NSF/NCAR C-130) and high-flying balloon (LPMA/DOAS and MIPAS/TELIS/mini-DOAS payload) observations (Ferlemann et al., 2000; Weidner et al., 2005; Kritten et al., 2010; Prados-Roman et al., 2011; Kreycy et al., 2013; Gratz et al., 2015; Ye et al., 2016; Stutz et al., 2017; Werner et al., 2017).

The major design criteria for airborne measurements are a small weight (several to tens of kilograms), a small power consumption (200 W), multiple channels of moderate spectral resolution (i.e. ranging from several tenths of nanometres in UV to several nanometres in NIR) for UV/vis/NIR analysis of the skylight received from nadir and simultaneously in scanning limb direction, stable optical imaging, and finally an easy to operate instrument, either by onboard operators (e.g. on HALO) or fully automated for deployments on unmanned aircrafts, such as the NASA Global Hawk (Stutz et al., 2017). On HALO the mini-DOAS instrument is installed in the unpressurised so-called "boiler room" located in the rear of the HALO aircraft, which is not accessible during the flight. While this position favours the aircraft's balance and weight distribution and provides more versatile options to assemble more maintenance-prone instruments within the cabin, it comes with the handicap of strongly changing ambient conditions to operate the instrument (i.e. boiler room temperatures may change from −30 °C during polar missions to +50 °C in tropical missions, and the ambient pressures may change between 1000 mbar at the ground and 150 mbar at cruise altitude), which are prohibitive for operating stable optical instrumentation. Therefore, we follow the proven concept of our airborne DOAS instrumentation, where the optical spectrometers are kept at vacuum pressures and temperature stabilised at 0 °C by immersing the whole spectrometer container into a water-ice vessel (Weidner et al., 2005). The latter also comes with the advantages of minimising the time ($\propto$ 2 h) to get the instrument flight-ready and larger auxiliary instrumentation (e.g. a cooler) is not necessary in the field.

The mini-DOAS instrument consists of three major parts (Fig. 1): (a) an aperture plate, from which three nadir and three limb scanning telescopes collect skylight and which is mounted into the aircraft fuselage; (b) a spectrometer unit,

which houses six cooled and evacuated grating spectrometers; and (c) a control unit to automatically operate the instrument and support communication with the aircraft data network.

2.1 The aperture plate and telescope

The aperture plate accommodates six telescopes in total for measurements in the UV (2 ×), visible (2 ×), and NIR (2 ×) spectral ranges. One set of UV/vis/NIR telescopes is used for limb and the other for nadir observations. It is mounted into an existing aperture opening ($28 \times 20.5 \times 9\,cm^3$) of the HALO aircraft fuselage and has a weight of about 4 kg. The three limb scanning telescopes point to the starboard side of the aircraft, perpendicular to the aircraft fuselage axis, and are moveable to attain elevation angles (EAs) from +3 to −93° relative to the horizon, in steps of less than 0.005°. During the flight they are commanded to compensate for the changing roll angle of the aircraft (see below), while the three nadir telescopes are held fixed. The six telescopes have diameters of 1.2 cm each, and six silica fiber bundles conduct the collected light from the telescopes to the spectrometers. At the spectrometer end, the fibers are linearly arranged and placed at the entrance slits of the spectrometers. At the telescope end, the fibers are linearly arranged and positioned in the focal point of the telescope lenses, forming fields of view of 3.15° in the horizontal and 0.38° in the vertical for both the UV and visible telescopes, and 1.68° in the horizontal and 0.76° in the vertical for the NIR telescopes (for the other details see Table 2). Finally, an industrial miniature camera is attached to the telescope aperture plate and oriented towards the sky's limb for monitoring of the investigated sky area simultaneously with the spectroscopic measurements.

2.2 Spectrometer unit

The six grating spectrometers are assembled in a Czerny–Turner configuration with the specifications given in Table 2. Back-thinned silicon CCDs with 2048 channels are employed for detection in the UV and visible wavelength range, while the NIR spectrometers use InGaAs photodiode arrays with 512 channels. In order to clearly identify each spectrometer and the corresponding telescope, they are labelled by the wavelength range and numbered 1 through 6. Spectrometers UV1, VIS3, and NIR5 (odd numbers) are then used in nadir-viewing geometry, and spectrometers UV2, VIS4, and NIR6 (even numbers) are used in limb-viewing geometry. All spectrometers are mounted on the lower side of the lid of a vacuum-tight container. The spectrometer container lid also accommodates vacuum-tight connectors and feedthroughs for the fiber bundles and the connection to the detector electronics. Prior to each mission the vacuum-tight spectrometer container is evacuated to some 10^{-5} mbar (leakage rate $2 \times 10^{-5}\,mbar\,L\,s^{-1}$) to keep the spectrometer and detectors clean from contamination and the optical imaging stable. The whole vacuum-tight spectrometer container is immersed into a vessel filled with 7 L of water/ice, in order to stabilise the spectrometer and detector temperatures at around 0 °C. The whole spectrometer unit is further insulated using a combination of silica vacuum insulation panels (thermal conductivity of $0.008\,W\,(m\,K)^{-1}$) and a more flexible polyvinylidene fluoride foam (thermal conductivity of $0.037\,W\,(m\,K)^{-1}$). Prior to a flight, the water-ice vessel is filled with 4 kg of ice and 3 L of cooled water, providing a latent heat of melting of 1300 kJ. Ambient conditions before the flight determine the amount of latent heat necessary to cool down the instrument and the heat flow into it on the ground. The instrument is cooled down usually between 1.5 and 2.5 h before takeoff due to pre-flight aircraft procedures. In consequence the holding time of the water ice against melting as well as the quality of stabilising the instrument temperature is somewhat variable, but it typically ranges between 6 and 8 h in a flight. When operating under arctic conditions, i.e. with an already cooled instrument prior to flight preparations, constant temperatures are maintained for 10 h or more, showing that average heat flows during operation are well below 36 W. In a worst-case scenario, i.e. in very hot and humid ambient conditions in the tropics (e.g. in Manaus, Brazil, in autumn 2014, or the Maldives in August 2015), the instrument has to be cooled additionally by adding ice and removing liquid water directly prior to the flight. Under these conditions, the average heat flow during flight preparation and measurement flight is around 80 W, and therefore in the present configuration the instrument is limited to 3–4 h of stable temperatures ($\Delta T \leq \pm 1$ °C). Therefore, after gaining some experience with the instrument's heat budget, three Peltier elements were additionally mounted on top of the spectrometer container lid.

2.3 Control unit

The power supply, the readout electronics for the six spectrometers, the controllers for the telescope motion, the control board for the Peltier elements, housekeeping electronics, and a single-board personal computer for instrument control and data storage and communication with the operator in the aircraft cabin are integrated into two removable electronic boxes, mounted above the spectrometer unit (yellow boxes in Fig. 1). The measurements and control processes including readout of the aircraft attitude data and the motion control of the three limb scanning telescopes are controlled by a LabView software running on the single-board computer. Finally the whole instrument is mounted on a custom-built rack of $45 \times 47 \times 54\,cm^3$. The total weight of the instrument is 57 kg, including the water/ice, and it consumes 100–200 W of 28 V DC power provided by the aircraft, depending on the power consumption of the Peltier elements.

Table 2. Optical specifications of the mini-DOAS instrument.

Channel name	UV	VIS	NIR
Telescope focal length and f number	30 mm, f/2.5		
Telescope lens coating	UV-AR	VIS 0°	NIR II
Telescope Schott filter type	BG3	GG400	RG850
Number of fibers and diameter	$7 \times 200\,\mu m$		$2 \times 400\,\mu m$
Fibre bundle entrance slit dimension	$1652\,\mu m \times 200\,\mu m$		$884\,\mu m \times 400\,\mu m$
$FOV_{opt}\ 2 \cdot \gamma$	$3.15° \times 0.38°$		$1.68° \times 0.76°$
Spectrometer entrance slit dimension	$1500\,\mu m \times 100\,\mu m$		$500\,\mu m \times 100\,\mu m$
Spectrometer focal length and f number	60 mm, f/4		
Grating (grooves/mm)	2100	1300	300
Sensor name	S10141-1107S		G9204-512
Sensor type	Si-CCD		InGaAs-PDA
Number of channels on sensor	2048		512
Sensor area per channel	$12 \times 1464\,\mu m^2$		$15 \times 500\,\mu m^2$
Full well capacity	$2 \times 10^5\ e^-$		$1.87 \times 10^8\ e^-$
Quantum efficiency*	0.60	0.85	0.80
Covered wavelength range	310–440 nm	420–640 nm	1100–1680 nm
Resolution (slit function FWHM)	0.47 nm/6.1 px	1.1 nm/8.4 px	≈ 10 nm/≈ 11 px

* Corresponding to the wavelengths of 400 nm (UV), 540 nm (VIS) or 1500 nm (NIR).

2.4 Pre-flight test measurements

Prior to each mission, the instrument is optically and electronically characterized in the laboratory. This characterisation includes recording of the dark currents and offset voltage of the CCD detectors, recording of line shapes and the optical dispersion, recording of trace gas absorption spectra, measurements of the telescope's fields of view, and alignment of telescopes to the major aircraft axis (roll angle).

Dark current and offset voltages of the CCD detectors are recorded prior to each flight for post-flight data processing (Platt and Stutz, 2008).

The spectrometer slit function and wavelength dispersion are monitored in the laboratory and in the field prior to each flight using HgNe and Kr emission lamps (see Table 2). Moreover, since test measurements in the laboratory show that the slit functions are sensitive to the spectrometer's temperature, their T dependence is extensively studied and monitored in the laboratory. For example, it is found that the width of the slit function is most sensitive at low temperatures, with a sensitivity of $0.005\,nm\,K^{-1}$ (0.04 channels K^{-1}). However, due to the thermal stability of the instrument, a temperature-sensitive slit function does not need to be taken into account for most spectral retrievals.

The effective FOV (FOV_{eff}) of the telescopes is made up of three contributions, which are (a) the optical FOV of the telescope (FOV_{opt}), (b) the lag time between aircraft movement and telescope attitude correction (Δ_{attit}), and (c) the backlash of the telescope gear (Δ_{gear}). These are discussed in the following paragraphs.

a. The optical FOV (FOV_{opt}) of the telescopes is measured in the laboratory prior to deployment of any mission. FOV_{opt} is listed in Table 2. The vertical FOV_{opt} in the UV/vis is $\approx 0.38°$.

b. In order to maintain the targeted EAs of the telescopes relative to the horizon during flight, the changing roll angle of the moving aircraft has to be corrected for. The aircraft's attitude data are received from the aircraft sensor data system (BAsic HALO Measurement And Sensor system, or BAHAMAS) aboard the HALO aircraft at a frequency of 10 Hz and a time delay < 1 ms via an Ethernet UDP broadcast. Due to the continuous movement of the aircraft and the time delay between data transmission and actual motor movement, a small difference between the targeted and the actual telescope angle can thus be expected. Tests involving a continuous and arbitrary sampling of the aircraft roll angle and the telescope position yield a mismatch of both angles with a standard deviation of $\Delta_{attit} \approx 0.17°$–$0.18°$ (Fig. S1 in the Supplement).

c. In addition, the pointing precision is limited by the backlash of the telescope's gear (Δ_{gear}). Telescope gear backlash ($\Delta_{gear} \approx 0.05°$) is determined by the shift of the recorded radiance maximum when the telescope's FOV is measured by scanning in opposite directions.

Gaussian summation of contributions (a)–(c) gives a FOV_{eff} for e.g. the VIS4 telescope ranging between 0.54° (during mission ML-Cirrus; Voigt et al., 2017) and 0.64° (during the TACTS/ESMVal mission; e.g. Müller et al., 2016).

After integration of the instrument into the aircraft, the telescope angle with respect to the aircraft is calibrated by placing a Ne gas lamp at a 15 m distance and at the same

Table 3. Details of the spectral analysis of various trace gases.

Target gas	λ (nm)	Fitted absorbers	Add. param.	Polyn.	σ (dSCD)
O_4	350–370	1, 2, 3, 5, 7, 9	I_{Ofs}[a], R[b], $R \cdot \lambda^4$[c]	2	
	460–490	1, 2, 4, 6	I_{Ofs}, R, $R \cdot \lambda^4$	2	5×10^{41}
O_3	335–362	1, 2, 4, 7, 9	I_{Ofs}, R, $R \cdot \lambda^4$	2	
	450–500	1, 2, 4, 6	I_{Ofs}, R, $R \cdot \lambda^4$	2	4×10^{18}
NO_2	407–435	1, 2, 3, 4, 6, 10	I_{Ofs}, R, $R \cdot \lambda^4$	2	
	424–490	1, 2/3, 4/5, 6	I_{Ofs}, R, $R \cdot \lambda^4$	2	2×10^{15}
H_2O	490–520	1, 2, 5, 6	I_{Ofs}, R, $R \cdot \lambda^4$	2	
HCHO	323–357	1, 2, 3, 5, 7, 8, 9	I_{Ofs}, R, $R \cdot \lambda^4$	2	7×10^{15}
HONO	337–372	1, 2, 3, 4, 7, 8, 9	I_{Ofs}, R, $R \cdot \lambda^4$	2	
BrO	342–363	1, 2, 3, 4, 7, 9	I_{Ofs}, R, $R \cdot \lambda^4$	2	2×10^{13}
OClO	353–392	1, 2, 3, 4, 10	I_{Ofs}, R, $R \cdot \lambda^4$	2	3×10^{13}

[a] I_{Ofs}: offset spectrum. [b] R: Ring spectrum. [c] $R \cdot \lambda^4$: Ring spectrum multiplied with λ^4.

height as the line of sight of the telescopes. The lamp is modified so that light is only emitted through a narrow (∼ 5 mm) slit. Scanning over the lamp again gives the FOV of the telescope, whose maximum is used to determine the angle that represents a horizontal line of sight with respect to the horizon. Under the assumption of a 2 cm uncertainty in the height of the lamp relative to the aperture plate (1 cm at each side), the angle uncertainty is 0.076°. When the aircraft is grounded, the aircraft roll angle given by the aircraft attitude data has a standard deviation of 0.2°. Accordingly, the systematic error in telescope alignment is $\Delta_{align} < 0.3°$.

The systematic misalignment (Δ_{align}) can be tested independently by observation of the radiance "knee", i.e. the apparent maximum in the relative radiances received from a set of EAs in limb direction, which is wavelength dependent (see Fig. 5 in Deutschmann et al., 2011, and Fig. 5 in Weidner et al., 2005). Figure S2 in the Supplement shows measured and modelled relative radiances in the UV and visible wavelength ranges, indicating a systematic misalignment below 0.2°. This accuracy is sufficiently narrow due to the widening of the effective FOV due to light scattering (as indicated by RT calculations, see e.g. Raecke, 2013; Knecht, 2015) and it is comparable to other stabilised airborne DOAS instruments (e.g. Baidar et al., 2013, Fig. 3).

3 Methods

3.1 DOAS retrieval

The spectral retrieval is based on the DOAS method (Platt and Stutz, 2008) and it is applied to measurements in the UV and visible wavelength ranges. The evaluation of measurements in the near-infrared is carried out using other approaches (Wolf et al., 2017; Scalone, 2017), which are not in the scope of this study. The primary product of the DOAS spectral retrieval in scattered sunlight applications are so-called differential slant column densities (dSCDs) given in molecules per cm^2 (Platt and Stutz, 2008), i.e. the amount of absorption measured in a foreground versus background spectrum. Since the details of the spectral retrieval and its uncertainties have been described in previous studies (Harder et al., 1998; Aliwell et al., 2002; Weidner et al., 2005; Dorf et al., 2006; Butz et al., 2006; Kritten et al., 2010; Stutz et al., 2017), here only those details are discussed which depart from our previous work. Table 3 provides a brief summary of the different DOAS settings and typical dSCD errors. Table 4 lists the absorption cross sections used in the analysis together with their uncertainties as stated in the literature. In all spectral retrievals a polynomial of degree 2 is included to compensate for broadband extinction features in the RT of the atmosphere, together with a background spectrum, a Ring spectrum, and an additional Ring spectrum multiplied by λ^4 as suggested by Wagner et al. (2009). The trace gas cross section spectra are calculated by convolving the literature absorption cross sections listed in Table 4 with the measured dispersion and a Gaussian line shape describing the Hg line at 404 nm (UV) or the Kr line at 450 nm (vis). Inaccuracies in wavelength calibration due to small changes in the instrument's optics and errors in the wavelength calibration of the fitted spectra are accounted for during the spectral retrieval. All trace gas cross sections are linked together and the package of trace gas cross sections is allowed to shift against the background spectrum and the Ring spectra which are linked together. Typical spectral shifts for both groups of spectra are well below one detector pixel.

3.1.1 Spectral retrieval of O_3, BrO, OClO, CH_2O, and O_4 in the UV spectral range

Five different spectral windows are analysed for the absorption of O_3, BrO, OClO, CH_2O, and O_4 in the UV wavelength

Table 4. Trace gas absorption cross sections used for the DOAS retrieval.

No.	Absorber	Temp.	Reference	Uncertainty
1	O_4	293 K	Thalman and Volkamer (2013)	4 %
2	O_3	223 K	Gorshelev et al. (2014), Serdyuchenko et al. (2014)	3 %
3	O_3	293 K	Gorshelev et al. (2014), Serdyuchenko et al. (2014)	3 %
4	NO_2	223 K	Bogumil et al. (2003)	3.4 %
5	NO_2	293 K	Bogumil et al. (2003)	3.4 %
6	H_2O	273 K	Rothman et al. (2009)	
7	HCHO	293 K	Chance and Orphal (2011)	5 %
8	HONO	298 K	Stutz et al. (2000)	5 %
9	BrO	223 K	Fleischmann et al. (2004)	10 %
10	OClO	213 K	Kromminga et al. (2003)	5 %

region (Tables 3 and 4). All five intervals are different but show significant overlap (Table 3).

O_3 is retrieved in the 335–362 nm wavelength region of the Huggins band in order to achieve a larger spectral overlap with the other targeted gases in the UV spectral range which is found necessary in support of the scaling method (see Sect. 3.6). Here O_3, BrO, NO_2, and O_4 references are included in the spectral retrieval (Table 3). The average error in the inferred O_3 dSCD is 6.4×10^{16} molec cm^{-2} for the UV spectral range. It is noteworthy that the spectral retrieval for O_3 could be improved by using the stronger ozone absorption bands of the Huggins band occurring towards the lower wavelength end of the UV spectrometer (310 nm), but then spectral overlap with the other gases as well as the much stronger absorption would negatively infer with the quality of the O_3-scaling method.

O_4 is retrieved in a spectral window ranging from 350 to 370 nm in order to allow fitting of the collisional band $^1\Sigma_g^+ + {}^1\Sigma_g^+(\nu = 1)$ (at 360.5 nm) (Table 3).

The BrO analysis window covers 342–362 nm, the vibrational transitions $3 \leftarrow 0$, $4 \leftarrow 0$, $5 \leftarrow 0$, and $6 \leftarrow 0$ of the $A^2\Pi_{3/2} \longleftarrow X^2\Pi_{3/2}$ electronic transition. Reference spectra of O_3 for 223 and 293 K (the latter orthogonalised to the 223 K reference spectrum) are included in the spectral retrieval together with reference spectra of NO_2, CH_2O, and O_4 (for the other parameters see Table 3). Figure 2 (bottom left) shows an example for the retrieval of BrO from a limb spectrum collected in the lowermost arctic stratosphere during the POLSTRACC mission (http://www.polstracc.kit.edu) on 31 January 2016. Here the BrO dSCD equals $(5.8 \pm 0.3) \times 10^{14}$ molec cm^{-2}.

OClO is retrieved in the 353–392 nm spectral range, i.e. of the vibrational bend and stretch transitions of the $A^2A_2 \longleftarrow X^2B_1$ electronic transition. The spectral fit includes reference spectra of O_3 at 223 and 293 K (the latter orthogonalised to the 223 K reference spectrum) as well as reference spectra of NO_2 and O_4. Figure 2 (bottom right) shows an OClO retrieval from the POLSTRACC flight on 31 January 2016. In this case the OClO dSCD is $(5.7 \pm 0.2) \times 10^{14}$ molec cm^{-2}.

CH_2O is retrieved in a spectral window ranging from 323 to 357 nm, i.e. the rovibrational bands of the $\widetilde{A}^1A_2 \longleftarrow \widetilde{X}^1A_1$ electronic transitions. The spectral window is chosen in order to distinguish the signature from other trace gas absorptions in this wavelength range, particularly of O_3, BrO, and HONO. The spectral retrieval includes absorption cross sections of O_3 at 223 and 293 K (the latter orthogonalised to the 223 K spectrum) and spectra of NO_2 and CH_2O taken at 293 K (since the bulk of CH_2O is expected to be present in the lower troposphere) as well as of O_4, HONO, and BrO. Figure 2 (top left) shows a sample CH_2O retrieval of a limb spectrum recorded during the HALO research flight above the Amazonian rain forest on 16 September 2014 performed within the framework of the ACRIDICON mission (Wendisch et al., 2016). In this case, the CH_2O dSCD amounts to $(1.28 \pm 0.05) \times 10^{17}$ molec cm^{-2}.

3.1.2 Spectral retrieval of O_3, O_4, NO_2, H_2O, IO, and $C_2H_2O_2$ in the visible spectral range

The main species measured in the visible spectral range are O_3, O_4, NO_2, and H_2O and, if sufficiently present, IO and $C_2H_2O_2$. Here the focus is put on the spectral retrieval of O_3, O_4, and NO_2, since the former two gases are used for the scaling method and the latter complements the measurements of NO and total NO_y by the AENEAS instrument (see Sect. 3.4.2) on board HALO. The spectral retrieval of IO, $C_2H_2O_2$, and water vapour is not discussed further in this paper.

Ozone is analysed in the 450–500 nm wavelength band of the Chappius absorption band. In the spectral retrieval, absorption cross sections of NO_2 at 223 K, together with O_4 and water vapour (Table 3), are included. The average error in the inferred O_3 dSCD is 4×10^{17} molec cm^{-2} in the visible spectral range.

The $^1\Sigma_g^+ + {}^1\Delta_g$ absorption of O_4 at 477.3 nm is analysed in the 460–490 nm wavelength band with the same combination of reference spectra as those used in the O_3 retrieval (Table 3). For O_4 the average retrieval error is 5.6×10^{41} molec^2 cm^{-5}.

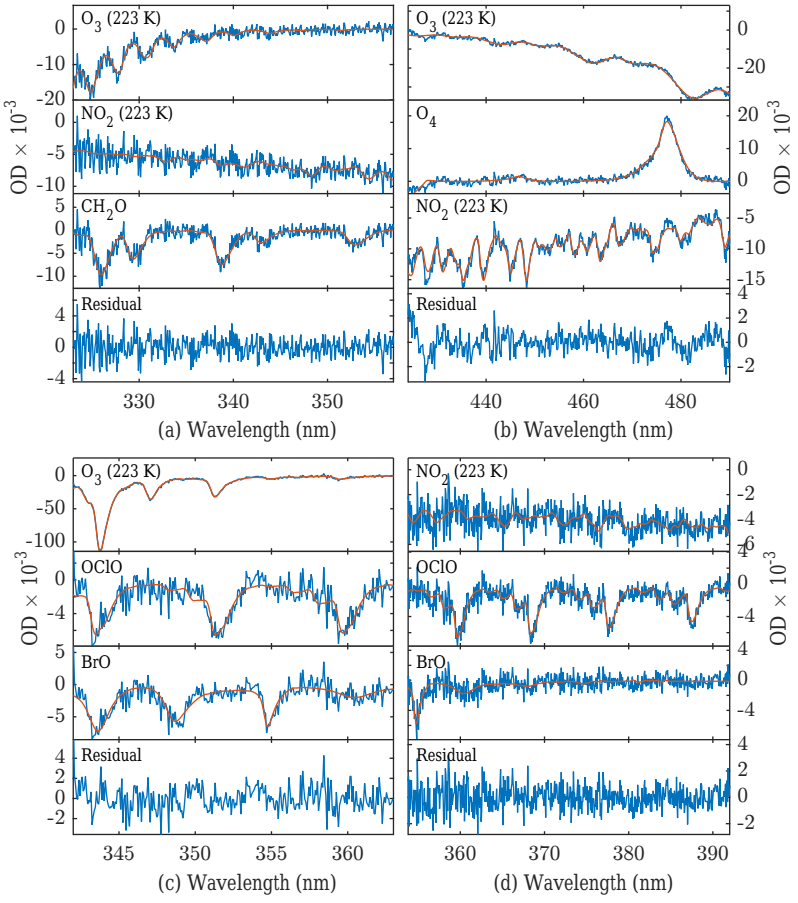

Figure 2. Sample spectral retrievals as described in Sect. 3.1. **(a)** CH_2O (1.4×10^{17} molec cm^{-2}) retrieval in the UV spectral range (ACRIDICON, 16 September 2014). **(b)** NO_2 (2×10^{16} molec cm^{-2}) retrieval in the visible spectral range (ESMVal, 13 September 2012). **(c)** BrO (8×10^{14} molec cm^{-2}) retrieval in the UV. **(d)** OClO (5.6×10^{14} molec cm^{-2}) in the UV (both POLSTRACC, 31 January 2016). Fitted reference absorption cross sections are shown in red and the residual structures are shown in blue.

NO_2 is analysed in a relatively wide spectral window ranging from 424 to 490 nm of the sub-bands of the electronic transition $^2B_1 \longleftarrow {}^2A_1$, thus supporting both small dSCD errors while maintaining a stability of the least squares fit involved in the spectral retrieval. The centre of both O_3 and O_4 fitting windows is thus shifted by 20 nm relative to NO_2. Reference spectra of O_3 at 223 and 293 K (the latter orthogonalised to the 223 K spectrum), O_4, and water vapour are included in the retrieval (Table 3). Figure 2 (top right) shows an example of a spectral retrieval of NO_2 with a dSCD of $(2.17 \pm 0.05) \times 10^{16}$ molec cm^{-2} for a limb spectrum taken within the framework of the ESMVal mission close to Antarctica on 13 September 2012. The simultaneous detection of O_3 and O_4 is also evident in this spectral retrieval.

3.2 Determination of the amount SCD_{ref}

In order to obtain the total slant column density (SCD), which is needed to solve the inversion problem, the amount of absorption SCD_{ref} contained in the background spectrum needs to be determined and added to the measured dSCD, i.e.

$$SCD = dSCD + SCD_{ref}, \quad (1)$$

where SCD_{ref} can be (a) determined using the so-called Langley method (i.e. a regression of dSCD as a function of total air mass), (b) inferred from a priori assumptions (for example for photolabile species like OClO $SCD_{ref} = 0$ can be reasonably assumed for high sun), or (c) simulated if the light paths (i.e. the optical state of the atmosphere) and the concentration field of the species are well known. As the mini-DOAS instrument is installed in the bottom of the aircraft fuselage, a direct sun light spectrum cannot be recorded, which prevents the use of method (a). Instead in most cases when methods (a) and (b) are not feasible, SCD_{ref} needs to be determined from the known RT and concentration field of the respective trace gas. For this purpose, flight sections with clear sky conditions are selected and a non-linear retrieval constrained by measured relative radiances and/or O_4 optical densities is carried out in order to infer the aerosol ex-

tinction (e.g. Prados-Roman et al., 2011; Stutz et al., 2017). The inferred aerosol profile and the a priori trace gas concentration profiles known for example from chemical modelling (Sect. 3.5) are then used in the RT modelling (see Sect. 3.3) to simulate SCD_{ref}. In order to obtain SCD_{ref} for flights where non-linear aerosol profile retrievals are not suitable, the measured spectra of these flights are fitted against a reference spectrum for which SCD_{ref} has previously been determined. The dSCD offset relative to the yet-undetermined reference spectrum is then used to calculate the missing SCD_{ref}. The uncertainty of SCD_{ref} is considerably decreased when the retrieval is referred to clear sky measurements. The largest dependencies of SCD_{ref} are the aerosol optical depth at flight altitude, the trace gas concentration at flight altitude, and the overhead column. Typical SCD_{ref} errors are of the order of 10–20 %.

3.3 Radiative transfer modelling

The RT is simulated in 2-D (and in selected cases in 3-D; see Fig. S3) using version 3.5 of the Monte Carlo RT model McArtim (Deutschmann et al., 2011). The model's input is chosen according to the onboard measured atmospheric temperatures and pressures, including climatological aerosol profiles from SAGE II (https://eosweb.larc.nasa.gov/project/sage2/sage2_v7_table) and Calipso (https://eosweb.larc.nasa.gov/project/calipso/cal_lid_l3_apro_cloudfree-standard-V3-00). The ground albedo is set to 0.15 over the sea and 0.3 over land, accounting for the surface reflectance and broken cloud cover. The RT model is further provided with the actual geolocation of the HALO aircraft, solar zenith and azimuth angles as encountered during each measurement, the telescopes azimuth and EAs, as well as the FOV of the mini-DOAS telescopes. Stutz et al. (2017) show in their Fig. 5 one example of simulated measurements for limb observations at about 18 km altitude. The simulations demonstrate that the Earth's sphericity, the correct treatment of atmospheric refraction, cloud cover, ground albedo, observation geometry, and wavelength dependency of scattering effects are relevant in the context of the interpretation of UV/vis/NIR limb measurements performed within the lower and middle atmosphere (Deutschmann et al., 2011). Even though the HALO mini-DOAS spectrometers are not radiometrically calibrated on an absolute scale, past comparison exercises with independently measured and McArtim simulated limb radiance provided confidence on the quality of the RT simulations (see Figs. 5 and 6 in Deutschmann et al., 2011; Fig. 2 in Kreycy et al., 2013; and Wolf et al., 2017).

For the forward simulations of the trace gas absorptions measured in limb direction, the RT model is run using simulated trace gas curtains along the flight track (for details see Sect. 3.5 and Fig. 3a and b). The term "curtain" is further on used to describe the magnitude of a (simulated) atmospheric parameter as a function of time/horizontal coordinate and altitude.

3.4 Additional measurements

3.4.1 FAIRO

FAIRO is a new, lightweight (14.5 kg) and accurate two-sensor device for in situ measuring O_3. It combines two techniques: (a) a UV photometer that measures the light absorption of O_3 at wavelengths of $\lambda = 250$–260 nm emitted by a UV-LED and (b) a chemiluminescence detector that monitors the chemiluminescence generated by O_3 on the surface of an organic dye adsorbed on dry silica gel (Zahn et al., 2012). Both techniques are simultaneously applied in order to combine the high measurement accuracy of UV photometry with the high measurement frequency of chemiluminescence detection. The UV photometer shows a 1σ precision of ~ 0.08 ppb at a measurement frequency of 0.25 Hz (and a pressure of 1 bar) and an accuracy of 1.5 % (determined by the uncertainty of the O_3 cross section). The chemiluminescence detector shows a precision of ~ 0.05 ppb at a measurement frequency of 12.5 Hz. In post-processing the chemiluminescence detector data are calibrated using the UV photometer data. FAIRO was first deployed on HALO during the TACTS/ESMVal mission (July to September 2012); its performance was excellent during all 13 flights.

3.4.2 AENEAS

NO and NO_y measurements on board HALO are performed using a two-channel chemiluminescence detector (AENEAS – Atmospheric nitrogen oxide measurement system) in combination with a catalytic conversion technique (Ziereis et al., 2000; Stratmann et al., 2016). A commercial two-channel chemiluminescence detector (ECO PHYSICS, Switzerland) is modified for use on board research aircrafts. The chemiluminescence technique is widely used for the detection of atmospheric NO and relies on the emission of light in the near-infrared following the reaction of NO with O_3 (e.g. Drummond et al., 1985). Heated gold tubes in combination with CO or H_2 as reducing agent are frequently used to convert all species of the odd nitrogen family (NO_2, HNO_2, HNO_3, HO_2NO_2, N_2O_5, PAN, etc.) into NO (e.g. Bollinger et al., 1983; Fahey et al., 1985), which is subsequently detected by chemiluminescence. The conversion efficiency of the gold converter is quantified using gas-phase titration of NO and O_3 before and after each flight with a conversion efficiency of typically more than 98 %. The statistical detection limit is 7 pmol mol^{-1} for the NO measurements and 8 pmol mol^{-1} for the NO_y measurements for an integration time of 1 s. The overall uncertainty for the NO and NO_y measurements is 8 % (6.5 %) for volume mixing ratios of 0.5 nmol mol^{-1} (1 nmol mol^{-1}).

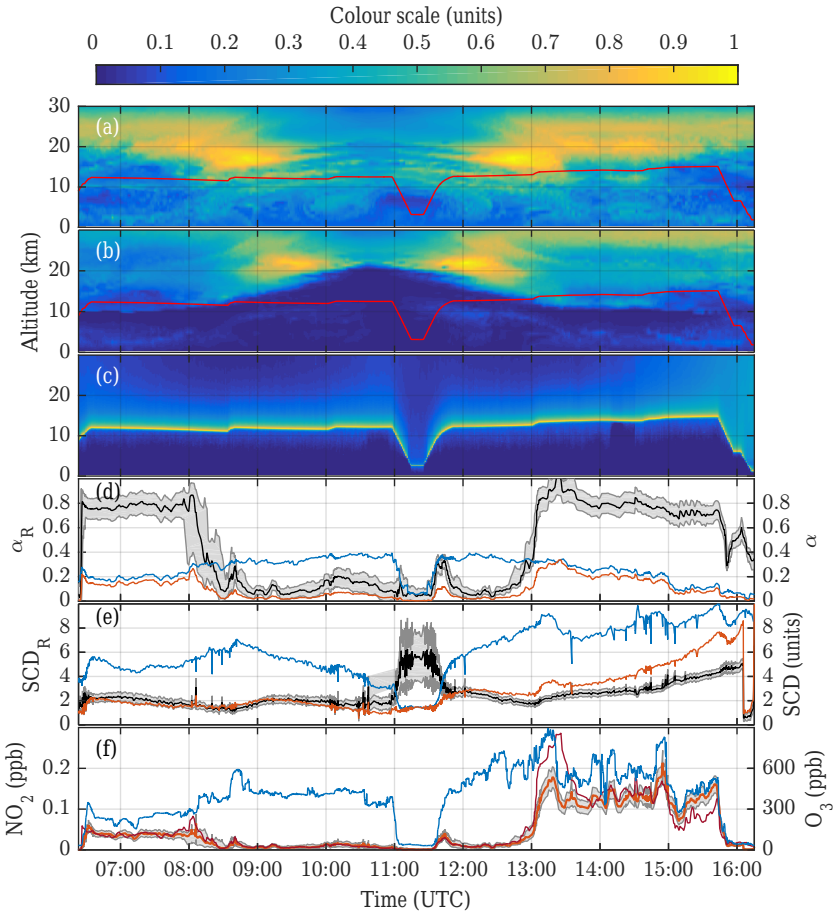

Figure 3. Illustration of NO_2 mixing ratio retrieval for the ESMVal flight on 13 September 2012 using the CTM CLaMS. **(a)** CLaMS-predicted [O_3] curtain (colour scale $\times\, 7.9 \times 10^{12}\,\mathrm{cm}^{-3}$) and aircraft altitude (red line). **(b)** CLaMS-predicted [NO_2] curtain (colour scale $\times\, 2.9 \times 10^{9}\,\mathrm{cm}^{-3}$) and aircraft altitude (red line). **(c)** BoxAMFs calculated by the RTM McArtim (colour scale $\times \log(217)$). **(d)** Calculated α_{O_3} (blue) and α_{NO_2} (red) as well as α_R (black line) and its uncertainty range (grey shaded area). **(e)** Retrieved SCD_{O_3} (blue, scale divided by 9.0×10^{20}) and SCD_{NO_2} (red, scale divided by 3.4×10^{17}) as well as SCD_R (black line, scale multiplied by 10^4) and its uncertainty range (grey shaded area). **(f)** Retrieved $[NO_2]_{O_3}$ (light red line) and its uncertainty range (grey shaded area) together with in situ measured O_3 (blue line). The dark red line shows the NO_2 mixing ratios predicted by the CLaMS model.

3.4.3 TRIHOP

The TRIHOP instrument is a three-channel Quantum Cascade Laser Infrared Absorption spectrometer (QCLAS) capable of the subsequent measurement of CO, CO_2, CH_4, and N_2O (Schiller et al., 2008; Müller et al., 2016). The instrument applies QCLAS in the mid-infrared with a multipass absorption cell (type White), which is kept at a constant pressure of $p = 30$ hPa and has a path length of 64 m and a volume of 2.7 L. During TACTS/ESMVal the instrument is in situ calibrated approx. every 30 min during the flights against a secondary standard of compressed ambient air. The mixing ratios of the secondary standard are determined before and after the mission in the laboratory against National Oceanic and Atmospheric Administration (NOAA) standards. Therefore, the in-flight calibrations allow us to identify and correct slow instrumental drifts in the post-flight data evaluation. The integration time for each species is 1.5 s at a duty cycle of 8 s, which finally limits the temporal resolution of the measurements. During TACTS/ESMVal TRIHOP CH_4 (N_2O) data achieved a 2σ precision of 10 (1.1) ppbv and stability of the instrument of 15 (2.2) ppbv, respectively, before applying the post-flight data correction. The total uncertainty relative to the working standard of 18 (2.5) ppbv can be regarded as an upper limit.

3.5 Chemistry transport and chemistry climate models

The output of the CTM CLaMS and the CCM EMAC are used in the present study. They differ in a number of ways, in particular in their representation of dynamical features of the atmosphere and the used chemistry schemes. The models are introduced in the following and their differences are

highlighted later in Sects. 3.7.2 and 4.2 in the context of the scaling method.

CLaMS is a Lagrangian CTM system developed at Forschungszentrum Jülich, Germany. The specific model setup is described in detail by Vogel et al. (2015). It is driven by horizontal winds from ERA-Interim reanalysis (Dee et al., 2011) provided by the European Centre for Medium-Range Weather Forecasts (ECMWF). The horizontal resolution is 100 km and the simulation period ranges from May 2012 until October 2012. It is initialised using satellite data from AURA-MLS and ACE-FTS as well as tracer–tracer correlations. For further details of the model simulation, see Vogel et al. (2015) and references therein. Due to its Lagrangian design, the model is especially good at representing trace gradients (e.g. the extratropical tropopause or the polar vortex edge). It should be noted that the present CLaMS simulation is not optimized in particular to reproduce photochemical processes in the lower troposphere. Therefore, the employed chemistry setup only contains reactions of importance within the stratosphere (Grooß et al., 2014) and it contains neither sources of larger hydro-carbon compounds (e.g. volatile organic compounds and non-methane hydrocarbons) nor any interactions of the chemical compounds with clouds.

The ECHAM/MESSy Atmospheric Chemistry (EMAC, http://www.messy-interface.org/) model is a numerical chemistry and climate simulation system that includes submodels describing processes in the troposphere and middle atmosphere and their interaction with oceans, land, and human influences (Jöckel et al., 2010). It uses the second version of the Modular Earth Submodel System (MESSy2) to link multi-institutional computer codes. The core atmospheric model is the fifth-generation European Centre Hamburg general circulation model (ECHAM5; Roeckner et al., 2006). Here, we analyse data of the RC1SD-base-10a simulation (Jöckel et al., 2016) sampled along the aircraft flight track with the submodel S4D (Jöckel et al., 2010). The time resolution is the model time step length, i.e. 12 min for the applied model resolution. For the RC1SD-base-10a simulation, EMAC has been nudged towards ERA-Interim reanalysis data (Dee et al., 2011) to reproduce the "observed" synoptic situation in the model (for details see Jöckel et al., 2016). The model is applied in the T42L90MA-resolution, i.e. with a spherical truncation of T42 (corresponding to a quadratic Gaussian grid of approx. 2.8 by 2.8° in latitude and longitude) with 90 vertical hybrid pressure levels up to 0.01 hPa. In contrast to CLaMS, EMAC contains a very detailed tropospheric chemistry scheme. The submodel MECCA (Module Efficiently Calculating the Chemistry of the Atmosphere; Sander et al., 2011a) is used to simulate the chemical kinetics, with the photochemical data taken from the JPL compilation (Sander et al., 2011b), including recent updates (Jöckel et al., 2016, Sect. 3.5).

3.6 The scaling method

The scaling method makes use of the information on the relevant RT gained from a simultaneously in situ and remotely (line-of-sight) measured scaling gas P and the remotely measured absorption of the target gas X to infer the absolute concentration $[X]$ (Raecke, 2013; Großmann, 2014; Werner et al., 2017; Stutz et al., 2017). Ideally, the absorption bands of X (e.g. NO_2) and P (O_3, O_4) are close to each other in order to diminish the influence of wavelength dependent Rayleigh and Mie scattering on the results (Table 3). The advantages of the scaling method over optimal estimation come from largely removing uncertainties in RT due to aerosols and clouds.

Mathematically, the method evolves along the following lines. The total measured SCD ($= \mathrm{dSCD} + \mathrm{SCD_{ref}}$) (Eq. 1) can be split into slant column densities ($[X]_i \cdot B_{X_i} \cdot z_i$) of individual atmospheric layers i of thickness z_i with concentrations $[X]_i$ and so-called box air mass factors (BoxAMFs) B_{X_i} for the targeted gas X (here BrO and NO_2) and the scaling gas P (here O_3 and O_4), i.e.

$$\mathrm{SCD}_X = \sum_i [X]_i \cdot B_{X_i} \cdot z_i, \tag{2}$$

$$\mathrm{SCD}_P = \sum_i [P]_i \cdot B_{P_i} \cdot z_i. \tag{3}$$

For the atmospheric layer of interest j, i.e. the altitude range around aircraft altitude where the limb line of sight penetrates through and most of the absorption is picked up, the concentrations for both gases can be expressed as

$$[X]_j = \frac{\mathrm{SCD}_X - \sum_{i \neq j} [X]_i \cdot B_{X_i} \cdot z_i}{B_{X_j} \cdot z_j}, \tag{4}$$

$$[P]_j = \frac{\mathrm{SCD}_P - \sum_{i \neq j} [P]_i \cdot B_{P_i} \cdot z_i}{B_{P_j} \cdot z_j}. \tag{5}$$

By noting that for weak absorbers (i.e. those with optical densities much smaller than unity), the BoxAMFs B_{X_j} and B_{P_j} are the same for both gases X and P when measured in the same wavelength range, the ratio of Eqs. (4) and (5) yields

$$\frac{[X]_j}{[P]_j} = \left(\frac{\mathrm{SCD}_X - \sum_{i \neq j} [X]_i \cdot B_{X_i} \cdot z_i}{\mathrm{SCD}_P - \sum_{i \neq j} [P]_i \cdot B_{P_i} \cdot z_i} \right). \tag{6}$$

Further, by defining so-called α factors (α_X and α_P), which describe the fraction of the absorption in layer j relative to the total atmospheric absorption for both gases, i.e.

$$\alpha_{X_j} = \frac{\mathrm{SCD}_X - \sum_{i \neq j}[X]_i \cdot B_{X_i} \cdot z_i}{\mathrm{SCD}_X} \quad (7)$$

$$= \frac{[X]_j \cdot B_{X_j} \cdot z_j}{\sum_i [X]_i \cdot B_{X_i} \cdot z_i} \quad (8)$$

and

$$\alpha_{P_j} = \frac{\mathrm{SCD}_P - \sum_{i \neq j}[P]_i \cdot B_{P_i} \cdot z_i}{\mathrm{SCD}_P} \quad (9)$$

$$= \frac{[P]_j \cdot B_{P_j} \cdot z_j}{\sum_i [P]_i \cdot B_{P_i} \cdot z_i}, \quad (10)$$

the main equation of the scaling method can be written as

$$[X]_j = \frac{\alpha_{X_j}}{\alpha_{P_j}} \cdot \frac{\mathrm{SCD}_X}{\mathrm{SCD}_P} \cdot [P]_j, \quad (11)$$

$$= \alpha_R \cdot \mathrm{SCD}_R \cdot [P]_j. \quad (12)$$

Here $[P]_j$ is the in situ measured concentration of the scaling gas (e.g. O_3, O_4), but averaged over the time of spectrum integration, and SCD_X and SCD_P are obtained from HALO mini-DOAS measurements using a DOAS fit and then Eq. (1). α_R and SCD_R are the ratios of the α factors (obtained from RT model simulations) and the SCDs, respectively. Equations (8) and (10) are solved using the calculated BoxAMFs B_{X_i} and B_{P_i} of atmospheric layer i (RT model described in Sect. 3.3) and the concentrations $[X]_i$ and $[P]_i$ from CTM/CCM predictions (Sect. 3.5).

Figure 3 displays the major ingredients going into the scaling method. It shows CLaMS-simulated curtains of concentrations of O_3 (panel a) and NO_2 (panel b), simulated BoxAMFs (panel c), and α factors for O_3 and NO_2 and their ratio ($\alpha_R = \frac{\alpha_{NO_2}}{\alpha_{O_3}}$) together with its uncertainty (panel d) for the HALO flight from Cape Town to Antarctica and back on 13 September 2012. Measured SCDs and their ratio are shown in panel (e) and the retrieved NO_2 mixing ratio in panel (f). The uncertainties displayed here are discussed in Sect. 3.7.

This flight is chosen to demonstrate the key features of the method and its sensitivity to various parameters. For this flight, leading from the southern subtropics/midlatitudes into Antarctica in spring, it is expected that (a) the overhead (stratospheric) O_3 and NO_2 concentrations largely vary in space and time, (b) the concentration of both gases at flight altitude is low, and (c) in particular NO_2 exhibits strong concentration gradients near the tropopause and between air outside and inside the polar vortex, thus providing a critical case to test the scaling method. For this flight the RT modelled α factors range from 0.03 to 0.4 for O_3 and 0.02 to 0.3 for NO_2, and α_R ranges from 0.05 to 0.9.

Even though the α factors are comparably small and largely varying in space and time, the comparison of in situ measured and remotely sensed O_3 indicates a fairly compact relation (Fig. 4), similar to other airborne limb measurements (e.g. Bruns et al., 2004; Baidar et al., 2013; Stutz et al., 2017, Fig. 9). Together with RT simulations (Raecke, 2013; Knecht, 2015) this provides confidence in the retrieval of flight level trace gas concentrations from UV/vis spectroscopy.

Evidently, the scaling and target gases are not detected at exactly the same wavelength but rather in overlapping wavelength bands. The λ dependence of α_R is investigated in separate sensitivity simulations. For that purpose α factors are calculated for the lower and upper wavelength end of the spectral retrieval for each gas. In agreement with Stutz et al. (2017), it is found that α_R may only change by as much as a few percent in our applications. Thus, the error is negligible as compared to the other errors discussed in the following section.

3.7 Errors of the scaling method

The errors and uncertainties of the scaling method fall into the categories of random (presumably Gaussian distributed) errors and systematic errors. The sources and magnitudes of both are discussed in the following.

3.7.1 Random errors of the scaling method

The random errors and sensitivities of the scaling method towards all input parameters are addressed by inspecting the Gaussian error propagation of Eq. (12). The uncertainty $\Delta[X]_j$ is calculated from

$$\Delta[X]_j = \left[\left(\frac{\Delta\alpha_R}{\alpha_R}\right)^2 + \left(\frac{\Delta\mathrm{SCD}_R}{\mathrm{SCD}_R}\right)^2 + \left(\frac{\Delta[P]_j}{[P]_j}\right)^2\right]^{0.5} \cdot [X]_j. \quad (13)$$

In the following we discuss the different contributions to $\Delta[X]_j$ in Eq. (13). The magnitudes of the contributions are summarised in Table 5.

$\Delta[P]_j$: when using in situ measured O_3 as scaling gas, the uncertainty $\Delta[P]_j$ is given by the uncertainty of the O_3 measurements (FAIRO, Sect. 3.4.1). For the comparison of in situ with limb-measured O_3 the low-frequency (0.25 Hz) precision is obviously most relevant, since the light paths in limb direction average over extended air masses and thus in situ measured O_3 needs to be averaged. At 1 bar the stated O_3 error by FAIRO is ≤ 1 % for $[O_3] = 40$ ppb. However, in this context more relevant are errors due to horizontal and vertical gradients in the $[O_3]$ which are considered below (see Sect. 3.7.1, paragraph on $\Delta\alpha_R$).

When using O_4 as scaling gas, the altitude- and temperature-dependent O_4 concentration (in terms of molec^2 cm^{-6}) can easily be calculated with an uncertainty of $\leq \pm 1$ % (Greenblatt et al., 1990; Pfeilsticker et al., 2001; Thalman and Volkamer, 2013).

$\left(\frac{\Delta\mathrm{SCD}_R}{\mathrm{SCD}_R}\right)^2 = \left(\frac{\Delta\mathrm{SCD}_P}{\mathrm{SCD}_P}\right)^2 + \left(\frac{\Delta\mathrm{SCD}_X}{\mathrm{SCD}_X}\right)^2$: the $\Delta\mathrm{SCD}_P$ and $\Delta\mathrm{SCD}_X$ errors each have two contributions, i.e. the dSCD

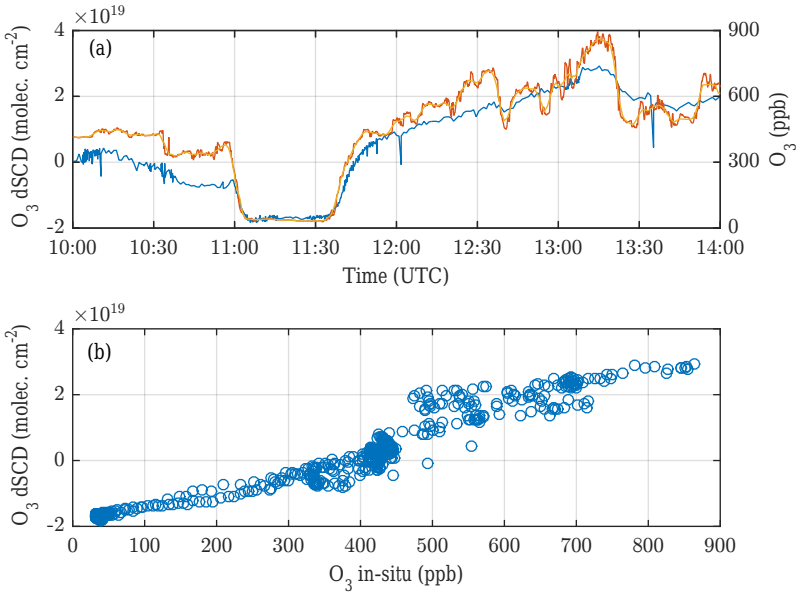

Figure 4. Comparison of in situ measured and remotely sensed O_3. **(a)** Time series of high time resolution (red line) and 5 min running average (orange line) of O_3 measured by the FAIRO instrument and remotely sensed O_3 (blue line) for a segment of the HALO flight from Cape Town to Antarctica on 13 September 2012. **(b)** Scatterplot of averaged in situ measurements and remotely sensed O_3 for the flight segment shown in **(a)**.

Table 5. Summary of random errors as discussed in Sect. 3.7.1. The percentages in columns three and four refer to deviations of the parameter in the first column.

Parameter	Cause of the error	Typical value	Maximum value
$\Delta\alpha_R$	RTM noise	3.5 %	3.5 %
	Mie scattering	10 %	15 %
	Small-scale variability	0–20 %	100 %
	Vertical sampling	0–10 %	60 %
$\Delta\mathrm{SCD}_R$	DOAS fit error	5 %	100 %
	Cross section	3 %	6 %
	$\mathrm{SCD}_{\mathrm{ref}}$	5–10 %	20 %
$\Delta[X]$	O_3 measurement	< 1 %	1 %
	O_4 calculation	1 %	1 %

errors due to the DOAS retrieval (Sect. 3.1) and the error in determining $\mathrm{SCD}_{\mathrm{ref}}$ (Sect. 3.2), which are added in quadrature. The dSCD error comprises the error of the spectral retrieval and the error of the trace gas cross section. Typical dSCD errors are mentioned in Sect. 3.1 and are often of the order of a few percent. Depending on the species, the $\mathrm{SCD}_{\mathrm{ref}}$ errors range from 1 to 20 %, but they are typically 10 % (see Sect. 3.2).

$\Delta\alpha_R$: the major contribution to the overall error $\Delta[X]_j$ may come from random errors in calculating α_R. In the following their uncertainties (ordered into contributions a, b, and c; see below) are subsequently addressed.

a. The error due to scattering by aerosols and clouds is studied from simulations of UV/vis limb measurements in a surrogate cloud field (Figs. S3 and S4 in the Supplement, and Knecht, 2015). Atmospheric parameters (temperature, pressure, and cloud cover) typical for the rainy season over the Amazon (e.g. Wendisch et al., 2016, and references therein) are assumed for the simulations, because such a scenario may represent the most severe disturbance of the radiative field in the UV/vis spectral range. The configuration of the cloud field is described in the Supplement (Fig. S3). For the cloudy sky, α_R is narrowly distributed within a range of typically $\Delta\alpha_R \leq \pm 5$ % around the clear sky case with some outliers within an interval of $\Delta\alpha_R \leq \pm 15$ % (Fig. S4 in the Supplement). A notable finding is that α_R follows the assumed concentration ratio of the target gas and

scaling gas, but by a somewhat damped amplitude, i.e. within an interval of $0.6 \leq \alpha_R \leq 1.8$, whereas the concentration ratio ranges between 0.2 and 1.7. In conclusion the scaling method thus largely removes the uncertainties in the concentration retrieval due the complexity of the RT in the UV/vis spectral range for a cloudy atmosphere. The modelled α_R depend on the relative profile shapes of the target gas and scaling gas but not on absolute concentrations. Overall this finding is in agreement with the recent findings of Stutz et al. (2017).

b. Uncertainties in α_R due to small-scale variability not covered by the CTM are addressed by a comparison of CLaMS-simulated and FAIRO-measured O_3 (Fig. S5 in the Supplement). For the HALO flight from Cape Town to Antarctica on 13 September 2012 CLaMS tends to systematically overpredict measured O_3 by up to 400 ppb, most likely due to errors in the vertical advection of the air masses in the sub-polar atmosphere. The impact of such a systematic error on the O_3 scaling is discussed below (see Sect. 3.7.2). Moreover, the difference of measured minus simulated $[O_3]$ clusters around several peaks with typical widths of $\Delta[O_3] \approx 40$ ppb, indicative of the sub-grid variability of $[O_3]$ not captured in the CLaMS simulations. Including the sub-grid variability in the α-factor calculation results in $\Delta\alpha_R < 0.1$ and a typical $\Delta\alpha_R \approx 0.05$. The same comparison for the retrieved NO_2 results in a typical sub-grid variability of 10 ppt and a similar $\Delta\alpha_R$ as for ozone.

c. The telescope FOV precision and pointing accuracy (Sect. 2.4) results in a rectangular window of about 500 m in height (at the location of maximum contribution to the radiance) from which the skylight is received. This is of the order of the vertical resolution of most CTMs and CCMs. It is therefore coherent to consider an uncertainty of ± 500 m of the altitude where the vertical profile is sampled. In order to test how this uncertainty propagates into $\Delta\alpha_R$ all simulated trace gas profiles are artificially shifted by 500 m upwards and downwards and the largest and lowest α_R are then used as uncertainty boundaries for each measurement geometry.

During most flight sections, $\Delta\alpha_R$ is dominated in equal parts by the uncertainty due to Mie scattering and sub-grid variability. However, if the vertical gradient of the involved trace gases is strong around flight altitude (e.g. at 08:00–09:00 UTC in Fig. 3), the vertical sampling uncertainty is the dominating effect (Fig. S6 in the Supplement). The resulting uncertainties are typically $\Delta\alpha_R \approx 10\,\%$–$20\,\%$ for O_3 and NO_2 and in rare cases of large vertical gradients up to $\Delta\alpha_R \approx 50\,\%$.

3.7.2 Potential systematic errors of the scaling method

In our study a priori information on the profile shapes is either taken from CTM/CCM modelling or, in the case of O_4, from calculations. It is thus necessary to consider how uncertainties in the predicted profile shapes propagate into the inferred concentrations at flight level.

Since a measure of the uncertainty of modelled trace gas profile shapes is not readily available, systematic errors of α_R are investigated by modifying the involved trace gas concentration profiles in two distinct ways: by (a) changing the concentration of the scaling gas to match the in situ measured concentration while keeping the concentration of the target gas at flight altitude fixed and (b) shifting the CTM/CCM-predicted concentration profiles of the scaling and target gas vertically in such a way that predicted N_2O concentrations at flight altitude agree with in situ measurements (Fig. S7 in the Supplement). It is found that errors (or biases) larger than the random error may occur if (a) the scaling gas concentration at flight altitude is significantly mispredicted by the models while the target gas concentration is not (or vice versa) or if (b) the CTM/CCM does not capture a strong vertical ascent/descent of air masses in a region with strong (and different) vertical concentration gradients of scaling and target gas. Both of these aspects need to be considered in the interpretation of measurements derived via the scaling method. For example, comparing predicted and measured concentrations of tropospheric tracers such as CH_4 and N_2O may give confidence in the representation of ascent/descent processes near the tropopause and thus justify confidence in the predicted trace gas profile shapes. A systematic error can also occur if the investigated trace gases exhibit strong horizontal gradients inside the volume sampled by the telescope's FOV, e.g. at the edge of a tropopause fold or the polar vortex. Thus, some caution is necessary when interpreting measurements close (tens of kilometres) to such gradients.

4 Sensitivity studies

Sensitivity studies regarding the employed scaling gas and the employed CTM/CCM are carried out for the ESMVal flight on 13 September 2012 leading from Cape Town southwards to 65° S and back. The lower edge of the Antarctic polar vortex was penetrated during the flight between approximately 08:00 and 13:00 UTC, i.e. south of 49° S. More information on the flight, in particular the transport of dehydrated air masses forming the Antarctic vortex into the upper and middle troposphere, can be found in the publication of Rolf et al. (2015).

4.1 Intercomparison of scaling with O_3 and O_4

We compare the inferred $[NO_2]$ for the HALO flight on 13 September 2012, using O_3 and O_4 as scaling gases. Figure 5 shows calculated α_R (panel a) and inferred $[NO_2]$ (panel b) using either O_3 (red symbols, further on denoted as $[NO_2]_{O_3}$) or O_4 (blue symbols, denoted as $[NO_2]_{O_4}$) as the scaling gas assuming clear skies (continuous lines) or a

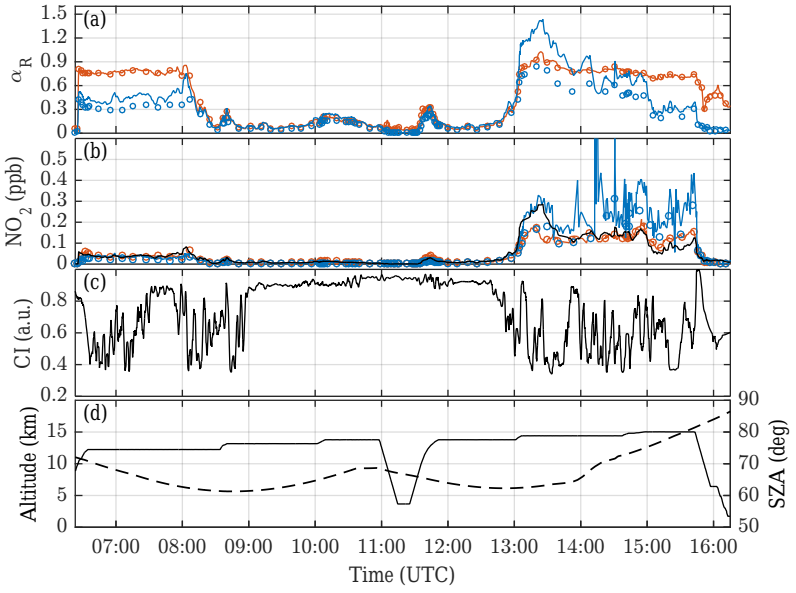

Figure 5. Retrieved $[NO_2]_{O_3}$ (red) and $[NO_2]_{O_4}$ (blue) for the ESMVal research flight on 13 September 2012. Calculations assuming clear skies are displayed as lines; calculations including a cloud layer at 4–8 km are displayed as circles. **(a)** Timeseries of calculated α_R. **(b)** Timeseries of inferred $[NO_2]$ together with NO_2 concentrations as predicted by CLaMs (black line). **(c)** Colour index (CI, 600 nm/430 nm radiances) observed by the VIS3 channel in nadir geometry. A large/small colour index indicates a cloud cover/clear sky below the aircraft, respectively. **(d)** Pressure altitude of HALO (black line) and solar zenith angle (SZA, black dashed line).

cloud layer (circles, description in the following paragraph) in the RT calculations. The retrieved $[NO_2]_{O_3}$ and $[NO_2]_{O_4}$ agree reasonably well before 13:00 UTC, exhibiting differences below 35 ppt and often as low as 10 ppt. The differences after 13:00 UTC come from the different sensitivities of O_3 and O_4 measurements towards the optical state (e.g. cloud cover) of the atmosphere. While the concentration of O_3 and NO_2 is largest in the stratosphere and usually smaller in the lower troposphere, it is the opposite for O_4. Therefore, the shielding effect of lower- and mid-level aerosols and clouds is expected to matter most for the limb detection of O_4 in the upper troposphere, but less for O_3 and NO_2.

The shielding effect of low- and mid-level aerosols and clouds is investigated by additional RT calculations considering an uniform cloud cover (optical thickness $\tau = 20$) located at 4–8 km altitude. The resulting α_R and inferred $[NO_2]$ are indicated as circles in panels (a) and (b) of Fig. 5. Evidently the cloud cover reduces α_R in O_4 scaling but does not significantly change α_R in O_3 scaling. Most striking is the influence of (broken) clouds on the O_4 scaling as evidenced by the large reduction in the calculated α_R for measurements prior to 08:00 UTC and after 13:00 UTC. Some proxy information on the cloud cover below the aircraft can be inferred from the colour index calculated from backscattered radiances at 600 nm/430 nm received by the nadir VIS3 channel (panel c in Fig. 5). Unlike for the time period between 09:00 and 12:30 UTC, when a more or less uniform cloud layer prevailed below the aircraft, the broken cloud cover past 13:00 UTC caused inferred $[NO_2]_{O_4}$ to become rather variable. In contrast $[NO_2]_{O_3}$ is much less variable and closely follows the CLaMS/EMAC-predicted $[NO_2]$, except for the period between 13:00 and 13:40 UTC. Here the inclusion of a cloud cover in the RT model causes $[NO_2]_{O_4}$ to converge towards $[NO_2]_{O_3}$.

Figure 6 shows the differences in inferred $[NO_2]_{O_3}$ and $[NO_2]_{O_4}$ profiles, assuming clear and cloudy skies. Evidently inferred $[NO_2]_{O_3}$ is much less sensitive to the cloud cover than $[NO_2]_{O_4}$. The small differences (mostly $< 5\,\%$) at higher altitudes for inferred $[NO_2]_{O_3}$ provide confidence in the $[NO_2]_{O_3}$ retrieval for the upper troposphere and lower stratosphere. In contrast, $[NO_2]_{O_4}$ is strongly dependent on assumptions regarding the cloud cover. These results are in agreement with those reported by Stutz et al. (2017). It is worth noting that within the Antarctic troposphere $[NO_2]$ is found to be rather low (< 20 ppt), and hence the systematic difference in the inferred $[NO_2]$ (up to 50 % for the $[NO_2]_{O_3}$ and up to 80 % for the $[NO_2]_{O_4}$) indicates the detection limit of the DOAS limb technique for NO_2.

In conclusion the profile shape dependence of the scaling method thus mandates to carefully choose the scaling gas; i.e. O_3 appears more appropriate as a scaling gas for the detection of gases of low tropospheric and large stratospheric abundance when probed from an aircraft flying in the middle and upper troposphere and lowermost stratosphere (e.g. such as NO_2, BrO) while O_4 appears to be more suited for gases of large concentrations in the lower troposphere (e.g. such as CH_2O, $C_2H_2O_2$, IO, and in polluted environments HONO and NO_2) when probed from low-flying airborne vehicles.

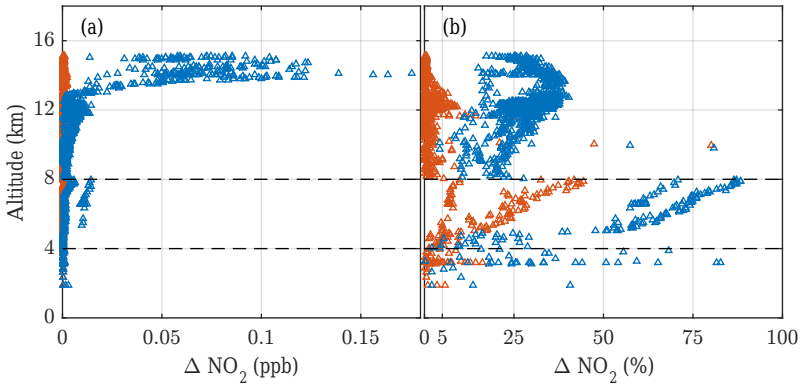

Figure 6. Impact of a cloud layer on retrieved $[NO_2]_{O_3}$ (red) and $[NO_2]_{O_4}$ (blue) for the ESMVal research flight on 13 September 2012. Shown are altitude profiles of the difference $\Delta[NO_2] = |[NO_2]_{clear} - [NO_2]_{clouded}|$ of the clear sky and clouded sky calculations, calculated from the data shown in Fig. 5b. The altitude range of the cloud layer as encountered during the dive and implemented in the clouded sky calculations is indicated by dashed lines.

4.2 EMAC versus CLaMS profile predictions

Next, the sensitivity of inferred $[NO_2]$ and [BrO] as a function of the predicted trace gas curtains is investigated. Mixing ratios are retrieved using trace gas curtains predicted by CLaMS (Fig. 3) and EMAC (Fig. 7).

The retrieved NO_2 mixing ratios agree within the random errors during most flight sections (Fig. 8b). However, some differences between the models have an impact on retrieval results, such as the higher spatial and temporal resolution of the CLaMS model. For example, a local maximum in $[NO_2]$ is predicted by CLaMS between 13:00 and 13:30 UTC but not by EMAC (Figs. 3 and 7, respective panel f, and Fig. 9c). The retrieved $[NO_2]$ using predicted O_3 from CLaMS (further on denoted $[NO_2]_{O_3,CLaMS}$) is $[NO_2]_{O_3,CLaMS} \approx 0.18 \pm 0.02$ ppb, while $[NO_2]_{O_3,EMAC} \approx 0.12 \pm 0.02$ ppb. Compared with the retrieved $[NO_2]$ for this period, the CLaMS prediction appears to be overestimated, while the EMAC prediction appears to be underestimated. Thus, model predictions with spatial resolutions comparable to the measurements (ca. 6 km horizontally) are desirable when applying the scaling method.

In the case of BrO, good agreement is reached in the range of 2–5 ppt in the extratropical lowermost stratosphere (flight sections A and E), but the difference between predicted $[BrO]_{O_3,CLaMS}$ and $[BrO]_{O_3,EMAC}$ is more substantial throughout flight sections B, C, and D (Figs. 8a and 9e). Two reasons for these differences can be identified. First, there is a discrepancy in predicted tropospheric BrO concentrations between the models, which leads to a difference in calculated α_{BrO} at all altitudes. Below 9 km altitude, CLaMS predicts 3–5 ppt, while EMAC predicts concentrations close to zero (Fig. 9b, dashed and dotted lines). This discrepancy is probably due to missing tropospheric sinks in the CLaMS model (Sect. 3.5). Hence, the EMAC-predicted [BrO] profile is expected to be more realistic. Secondly, while the extent of the polar vortex is predicted roughly in the same manner, the treatment of subsidence and methane degradation differs between the models. This can be observed by comparing measured and predicted methane mixing ratios in flight sections B and D (Figs. 8c and 9g). For both flight sections measurements indicate air mass ages up to 4.5 years in combination with strong dehydration (Rolf et al., 2015) and denitrification (Jurkat et al., 2017). However, the subsidence of O_3 appears to be overestimated in the CLaMS model, since the vertical profile of measured O_3 concentrations is more accurately represented by EMAC (Fig. 9a).

In conclusion, differences in relative profile shapes predicted by the employed models and their spatial and temporal resolution influence the retrieval results of the scaling method. These differences are particularly large when fundamental properties of the atmosphere, e.g. the presence of BrO in the troposphere or the subsidence in the polar vortex, are treated differently by the models. In most cases, inferred mixing ratios agree, independent of which model predictions (CLaMS vs. EMAC) are used.

5 Sample results and discussion

Finally, we discuss the mini-DOAS observations from the flight on 13 September 2012 in the context of complementary measurements and model predictions (Figs. 8 and 9). Besides the mini-DOAS measurements of O_3, NO_2, and BrO, complementary instrumentation provided information on the following gases: O_3 from the FAIRO instrument, NO and total NO_y from the AENEAS instrument, and CO and CH_4 from the TRIHOP instrument (Sect. 3.4). These measurements are further compared with the predictions of CLaMS and EMAC, which support the interpretation with respect to the atmospheric dynamics and photochemistry. Most notable is the joint detection of NO, NO_2, and total NO_y (and of BrO) in a remote location, such as in the Antarctic tropo-

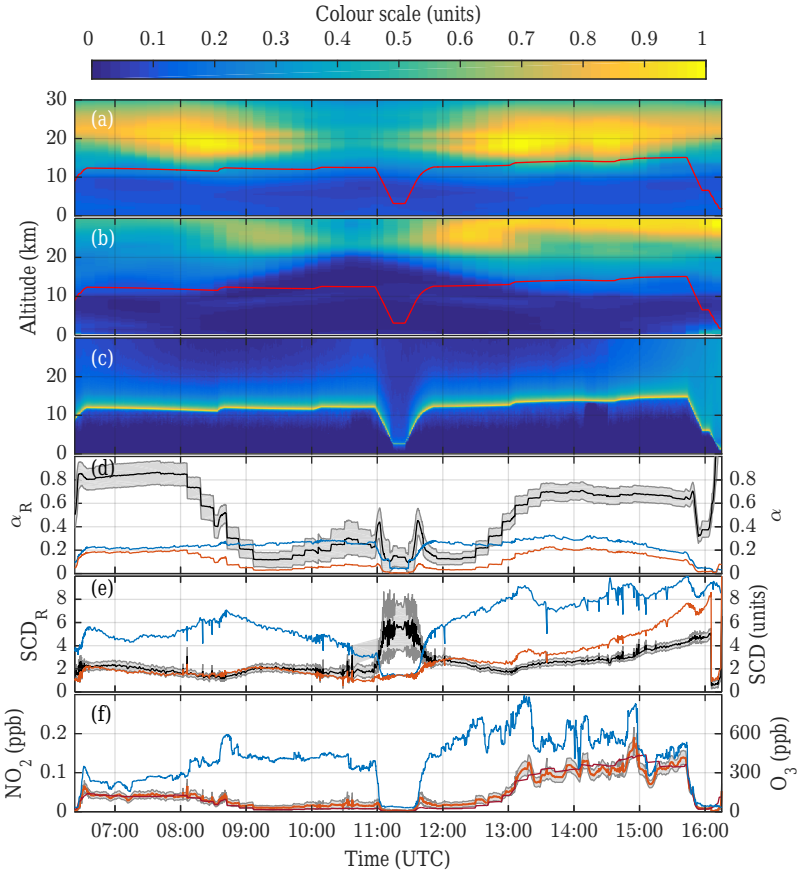

Figure 7. Illustration of NO_2 mixing ratio retrieval for the ESMVal flight on 13 September 2012 using the CCM EMAC. **(a)** EMAC-predicted $[O_3]$ curtain (colour scale $\times\, 7.9\times10^{12}$ cm^{-3}) and aircraft altitude (red line). **(b)** EMAC-predicted NO_2 curtain (colour scale $\times\, 2.9\times 10^9$ cm^{-3}) and aircraft altitude (red line). **(c)** BoxAMFs calculated by the RTM McArtim (colour scale $\times \log(217)$). **(d)** Calculated α_{O_3} (blue) and α_{NO_2} (red) as well as α_R (black line) and its uncertainty range (grey shaded area). **(e)** Retrieved SCD_{O_3} (blue, scale divided by 9.0×10^{20}) and SCD_{NO_2} (red, scale divided by 3.4×10^{17}) as well as SCD_R (black line, scale multiplied by 10^4) and its uncertainty range (grey shaded area). **(f)** Retrieved $[NO_2]_{O_3}$ (light red line) and its uncertainty range (grey shaded area) together with in situ measured O_3 (blue line). The dark red line shows the NO_2 mixing ratio predicted by the EMAC model.

sphere and lowermost stratosphere, since such measurements are infrequent or to date not existing. Overall, mixing ratios of BrO and NO_2 are inferred for the whole flight with a time resolution of 30 s and a resulting spatial resolution of $\sim$ 6 km, although RT implies further averaging along the line of sight (perpendicular to flight direction) of $\sim$ 200 km and along flight direction of $\sim$ 10 km. The detection limits for the measurements shown here are estimated by inspecting the uncertainty at very low mixing ratios, e.g. during the dive (Fig. 9c and e). For $[BrO] = 2$ ppt and $[NO_2] = 10$ ppt, respectively, the inferred mixing ratios are at least two times larger than the uncertainty. Measurements of CH_4, which is well mixed in the troposphere and is lost in the stratosphere, provide a measure of stratospheric age of the air. Accordingly, the flight is subdivided into five flight sections, A–E (Fig. 8c), in order to distinguish data recorded in the midlatitude lowermost stratosphere (flight sections A and E), polar winter vortex air (flight sections B and D), and the polar troposphere (flight section C). In September 2012 the tropospheric CH_4 mixing ratio at Cape Grim, Tasmania, was 1778 ppb (http://www.csiro.au/greenhouse-gases/).

Inferred BrO mixing ratios are around 4 ppt / 7 ppt in flight section B and 6 ppt / 8 ppt in flight section D, based on retrievals using CLaMS/EMAC in the scaling method, respectively (panel a of Fig. 8; differences between both retrievals are discussed above in Sect. 4.2). These concentrations are on the higher end of comparable BrO measurements in the same altitude range (12–13 km) reported in the literature (Harder et al., 1998; Dorf et al., 2006; Hendrick et al., 2007; Werner et al., 2017), which could be caused by the subsidence of stratospheric air from higher altitudes discussed above. Panel (e) of Fig. 9 shows the vertical BrO profile retrieved from the ascent of the dive at 65° S. The retrieved $[BrO]_{O_3,EMAC}$ and $[BrO]_{O_3,CLaMS}$ are both below the detection limit of 2 ppt in the altitude range below 9.5 km, even when using RT calculations based on CLaMS, which pre-

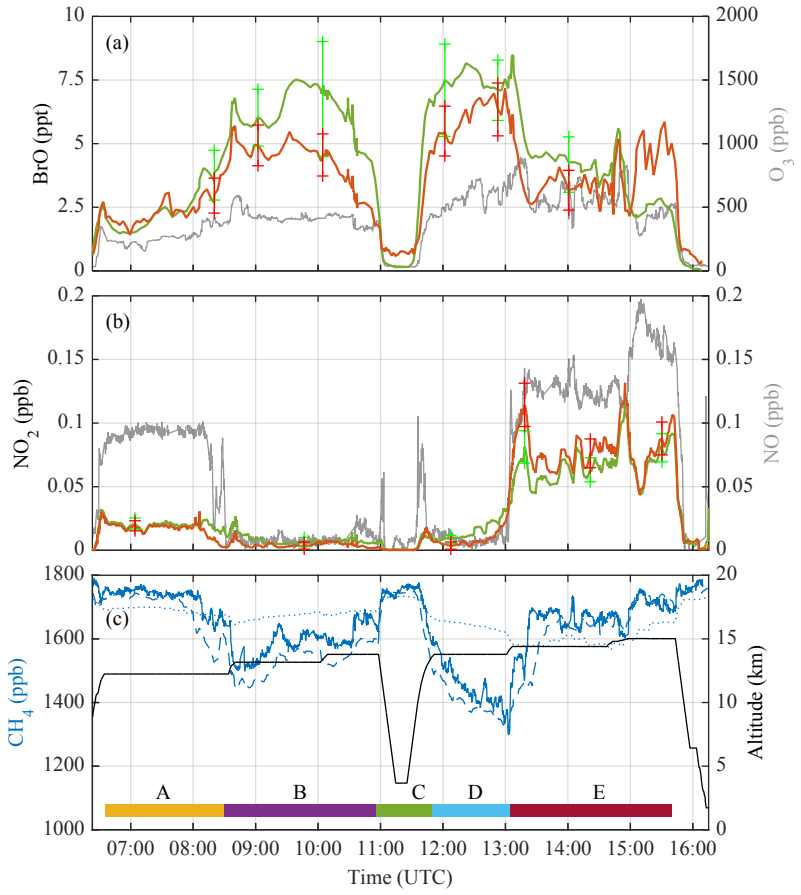

Figure 8. Time series of measured trace gas mixing ratios recorded during the ESMVal research flight on 13 September 2012. **(a)** In situ measured concentration of O_3 (grey) and inferred $[BrO]_{O_3}$ using profile shape predictions by CLaMS (red) and EMAC (green). **(b)** In situ measured NO (grey) and inferred $[NO_2]_{O_3}$ using profile shape predictions by CLaMS (red) and EMAC (green). The uncertainties are discussed in Sect. 3.7.1. **(c)** Pressure altitude of HALO (black) and CH_4 mixing ratios (blue), the latter as derived from in situ measurements by TRIHOP (continuous line), CLaMS prediction (dashed line), and EMAC prediction (dotted line). Additionally, flight sections A through E are marked for reference in the text.

dicts 3 ppt BrO in the troposphere. Hence, below 9.5 km altitude BrO could not be detected above the detection limit. The amount and distribution of halogen oxides such as BrO (panel e) in the troposphere is a matter of current debate (Harder et al., 1998; Fitzenberger et al., 2000; Van Roozendael et al., 2002; Saiz-Lopez and von Glasow, 2012; Volkamer et al., 2015; Wang et al., 2015; Schmidt et al., 2016; Sherwen et al., 2016; Werner et al., 2017) and is of significant scientific interest due to its potential influence on tropospheric ozone chemistry (von Glasow et al., 2004) and thus radiative forcing (Sherwen et al., 2017). Reported tropospheric background profiles at polar latitudes include those by Fitzenberger et al. (2000), who derive tropospheric BrO profiles above Kiruna (Sweden) from balloon measurements and conclude that tropospheric [BrO] amounting to 0.4–2.3 ppt was present, assuming a uniform distribution within the troposphere. Prados-Roman et al. (2011) use airborne DOAS measurements based in Spitzbergen to derive a BrO mixing ratio profile in Arctic spring with 15 ppt in the planetary boundary layer, 1.5 ppt in the free troposphere, and up to 6 ppt at 10 km in the lowermost stratosphere. The measurements derived in the present study are compatible with these previously inferred background profiles and do not show elevated BrO concentrations in the Antarctic free troposphere in September 2012.

Retrieved NO_2 (Fig. 8b) exhibits similar features as the independently measured NO. In polar vortex air (flight sections B and D), $[NO_2]$ is mostly between 5 and 20 ppt, i.e. near or below the detection limit of 10 ppt, similar to the in situ measured [NO]. Such small amounts of NO_x limit the deactivation of active chlorine, i.e. the formation of $ClONO_2$, and thus prolong ozone destruction in the polar winter vortex air. Interestingly, enhanced NO_2 together with increased NO are detected in the free troposphere (9–13 km altitude) during the dive (Fig. 9b and c). The largest [NO] of 60–80 ppt is measured in the altitude range of 10–12 km, while

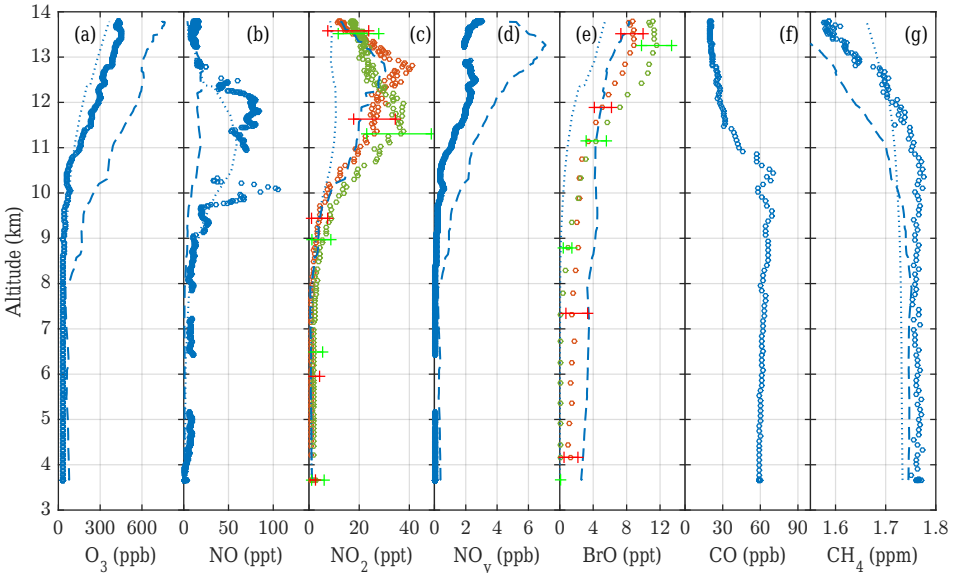

Figure 9. Altitude profiles of trace gas concentrations measured during the ascent (65° S, 21° E) of flight section C of the ESMVal research flight on 13 September 2012. **(a)** Measurements of O_3 (FAIRO), **(b)** NO (AENEAS), **(c)** NO_2 (mini-DOAS), NO_y (AENEAS, **d**), BrO (mini-DOAS instrument, **e**), CO (TRIHOP, **f**), and CH_4 (TRIHOP, **g**) are shown. **(a, b, d, f, g)** In situ measurements are indicated as blue circles, CLaMS predictions as dashed lines, and EMAC predictions as dotted lines. **(c, e)** Inferred $[NO_2]_{O_3}$ and $[BrO]_{O_3}$ (circles), respectively, with random errors (error bars) using profile shapes predicted by CLaMS (red symbols) and EMAC (green symbols).

the largest $[NO_2]$ of 30–40 ppt is inferred at altitudes of 11–13 km. Increased NO_2 concentrations are also predicted by the CLaMS model (Fig. 3b), indicating in-mixing of tropospheric air from more NO_x-rich air masses. Rolf et al. (2015) also infer in-mixing of moister midlatitude air into the bottom of the polar vortex, albeit not at the same time during the flight, since the used instrument (GLORIA) was switched off during the dive. At altitudes below 9 and 10 km, respectively, retrieved [NO] and $[NO_2]$ are near their detection limits of 7 and 10 ppt, indicating very pristine air.

6 Conclusions

We describe a novel six-channel optical spectrometer for airborne limb and nadir detection of UV/visible/NIR absorbing gases (e.g. O_3, O_4, NO_2, HONO, CH_2O, $C_2H_2O_2$, BrO, IO, OClO), liquid and solid water as well as of skylight radiances. Further, features of a novel retrieval method (called scaling method) are discussed which go beyond those recently reported by Stutz et al. (2017) and Werner et al. (2017). Here we demonstrate how absolute concentrations of the UV/vis absorbing gases can be inferred from limb measurements in the troposphere and lower stratosphere under all (clear and cloudy) skies. The scaling method largely avoids ambiguities in the necessary mathematical inversion to interpret the limb measurements which are introduced by the complexity of RT in the UV/vis spectral range for cloudy and heavily aerosol-loaded atmospheres. Instead, the relative profile shapes of the scaling gas and the target gas are the main a priori information used in the scaling method. Thus, uncertainties in the trace gas retrieval are primarily due to uncertainties in the relative profile shapes, which can be minimised when the retrieval uses a priori profile shapes for example from CTM/CCM predictions, calculations (e.g. O_4), or otherwise available measurements. The present study examines the resulting random and systematic errors of trace gas concentrations retrieved via the scaling method. The random error is estimated to be 10–20 % for most measurement conditions, dominated in equal parts by uncertainties due to Mie extinction and small-scale variabilities of the concentrations of the involved trace gases. The random error is comparatively large close to strong vertical or horizontal trace gas concentration gradients. Systematic biases can occur when trace gas profile shapes are strongly misrepresented by model predictions. Thus, comparing independent trace gas measurements of e.g. tropospheric or stratospheric tracers with model predictions is essential in the interpretation of retrieval results. For limb measurements in the upper troposphere and lower stratosphere the comparison of both scaling gases indicates a sensitivity of O_4 scaling for low clouds, while the O_3 scaling is insensitive. This is consistent with the expectation that a scaling gas with similar profile shape as compared to the target gas is best suited for the method. The comparison of retrievals involving a CTM (CLaMS) and a CCM (EMAC) reveals that results are in agreement within the random error, as long as the fundamental properties of the atmosphere are represented in a similar way (e.g. a presence or absence of a trace gas in the troposphere). Further, the comparison indi-

cates that CTM/CCM curtains with spatial resolutions close to those of the measurements are desirable.

The present study shows the applicability of the scaling method to HALO mini-DOAS measurements of NO_2 and BrO under all sky conditions. The scaling method replaces the constraint on RT used in the traditional optimal estimation (e.g. O_4 to infer the aerosol and cloud profile) by a scaling factor to estimate effective light path lengths (derived from relative trace gas profile shapes and RT modelling). The latter approach has the advantages that (a) trace gas concentration profiles are more homogeneous in space and time on the scales relevant for airborne DOAS measurements than cloud patterns and (b) the former can be predicted more reliably by modern CTMs/CCMs as compared to the presence of aerosols and clouds. Thus, the scaling method provides a novel and reliable means for inferring trace gas concentrations from airborne UV/vis limb measurements. The significantly decreased dependency on aerosol and cloud properties increases the ability to make use of already recorded data and decidedly widens the applicability of airborne UV/vis limb spectroscopy as a means of investigating atmospheric photochemistry.

Data availability. The data are available at https://halo-db.pa.op.dlr.de/mission/14.

The Supplement related to this article is available online at https://doi.org/10.5194/amt-10-4209-2017-supplement.

Competing interests. The authors declare that they have no conflict of interest.

Special issue statement. This article is part of the special issue "The ACRIDICON-CHUVA campaign to study deep convective clouds and precipitation over Amazonia using the new German HALO research aircraft (ACP/AMT inter-journal SI)". It is not associated with a conference.

Acknowledgements. This study was funded through the Deutsche Forschungsgemeinschaft, DFG (HALO-SPP 1294 and grants PF-384/7-1, PF-384/7-2, PF384/9-1, PF384/9-2, and PF-384/16-1). Additional funding from EU-SHIVA (FP7-ENV-2007-1-226224) is highly acknowledged. The authors gratefully acknowledge the computing time granted on the supercomputer JURECA at Jülich Supercomputing Centre (JSC) under the VSR project ID JICG11. The EMAC simulations have been performed at the German Climate Computing Centre (DKRZ) through support from the Bundesministerium für Bildung und Forschung (BMBF). DKRZ and its scientific steering committee are gratefully acknowledged for providing the HPC and data archiving resources for this consortial project ESCiMo (Earth System Chemistry integrated Modelling). We thank the Deutsches Zentrum für Luft- und Raumfahrt (DLR) for the support to get the instrument certificated and the DLR Flugexperimente Team at Oberpfaffenhofen, in particular Heinrich Brockstieger, Frank Probst, Martina Hierle, and Andrea Hausold, for the support given during the TACTS/ESMVal, NARVAL, ML-Cirrus, ACRIDICON, OMO, and POLSTRACC missions. We also thank Ralph Pfeifer from IUP Heidelberg for his ideas and technical support on behalf of the project.

Edited by: Stuart A. Penkett
Reviewed by: two anonymous referees

References

Aliwell, S. R., Van Roozendael, M., Johnston, P. V., Richter, A., Wagner, T., Arlander, D. W., Burrows, J. P., Fish, D. J., Jones, R. L., Tørnkvist, K. K., Lambert, J.-C., Pfeilsticker, K., and Pundt, I.: Analysis for BrO in zenith-sky spectra: An intercomparison exercise for analysis improvement, J. Geophys. Res.-Atmos., 107, ACH10-1–ACH10-20, https://doi.org/10.1029/2001JD000329, 2002.

Baidar, S., Oetjen, H., Coburn, S., Dix, B., Ortega, I., Sinreich, R., and Volkamer, R.: The CU Airborne MAX-DOAS instrument: vertical profiling of aerosol extinction and trace gases, Atmos. Meas. Tech., 6, 719–739, https://doi.org/10.5194/amt-6-719-2013, 2013.

Beirle, S., Boersma, K. F., Platt, U., Lawrence, M. G., and Wagner, T.: Megacity Emissions and Lifetimes of Nitrogen Oxides Probed from Space, Science, 333, 1737–1739, https://doi.org/10.1126/science.1207824, 2011.

Bogumil, K., Orphal, J., Homann, T., Voigt, S., Spietz, P., Fleischmann, O., Vogel, A., Hartmann, M., Kromminga, H., Bovensmann, H., et al.: Measurements of molecular absorption spectra with the SCIAMACHY pre-flight model: instrument characterization and reference data for atmospheric remote-sensing in the 230–2380 nm region, J. Photoch. Photobio. A, 157, 167–184, 2003.

Bollinger, M. J., Sievers, R. E., Fahey, D. W., and Fehsenfeld, F. C.: Conversion of nitrogen dioxide, nitric acid, and n-propyl nitrate to nitric oxide by a gold-catalyzed reduction with carbon monoxide, Anal. Chem., 55, 1980–1986, 1983.

Brandtjen, R., Klüpfel, T., Perner, D., and Knudsen, B. M.: Airborne measurements during the European Arctic Stratospheric Ozone Experiment: Observation of OClO, Geophys. Res. Lett., 21, 1363–1366, https://doi.org/10.1029/93GL01868, 1994.

Bruns, M., Buehler, S. A., Burrows, J. P., Heue, K.-P., Platt, U., Pundt, I., Richter, A., Rozanov, A., Wagner, T., and Wang, P.: Retrieval of profile information from airborne multiaxis UV-visible skylight absorption measurements, Appl. Optics, 43, 4415–4426, https://doi.org/10.1364/AO.43.004415, 2004.

Bruns, M., Buehler, S. A., Burrows, J. P., Richter, A., Rozanov, A., Wang, P., Heue, K. P., Platt, U., Pundt, I., and Wagner, T.: NO_2 Profile retrieval using airborne multi axis UV-visible skylight absorption measurements over central Europe, Atmos. Chem. Phys., 6, 3049–3058, https://doi.org/10.5194/acp-6-3049-2006, 2006.

Butz, A., Bösch, H., Camy-Peyret, C., Chipperfield, M., Dorf, M., Dufour, G., Grunow, K., Jeseck, P., Kühl, S., Payan, S., Pepin, I., Pukite, J., Rozanov, A., von Savigny, C., Sioris, C., Wagner, T., Weidner, F., and Pfeilsticker, K.: Inter-comparison of stratospheric O_3 and NO_2 abundances retrieved from balloon borne direct sun observations and Envisat/SCIAMACHY limb measurements, Atmos. Chem. Phys., 6, 1293–1314, https://doi.org/10.5194/acp-6-1293-2006, 2006.

Chance, K. and Orphal, J.: Revised ultraviolet absorption cross sections of H_2CO for the HITRAN database, J. Quant. Spectrosc. Ra., 112, 1509–1510, 2011.

Dee, D. P., Uppala, S. M., Simmons, A. J., Berrisford, P., Poli, P., Kobayashi, S., Andrae, U., Balmaseda, M. A., Balsamo, G., Bauer, P., Bechtold, P., Beljaars, A. C. M., van de Berg, L., Bidlot, J., Bormann, N., Delsol, C., Dragani, R., Fuentes, M., Geer, A. J., Haimberger, L., Healy, S. B., Hersbach, H., Hólm, E. V., Isaksen, L., Kållberg, P., öhler, M., Matricardi, M., McNally, A. P., Monge-Sanz, B. M., Morcrette, J.-J., Park, B.-K., Peubey, C., de Rosnay, P., Tavolato, C., Thépaut, J.-N., and Vitart, F.: The ERA-Interim reanalysis: configuration and performance of the data assimilation system, Q. J. Roy. Meteor. Soc., 137, 553–597, https://doi.org/10.1002/qj.828, 2011.

Deutschmann, T., Beirle, S., Frieß, U., Grzegorski, M., Kern, C., Kritten, L., Platt, U., Pukite, J., Wagner, T., Werner, B., and Pfeilsticker, K.: The Monte Carlo Atmospheric Radiative Transfer Model McArtim: Introduction and Validation of Jacobians and 3D Features, J. Quant. Spectrosc. Ra., 112, 1119–1137, 2011.

Dix, B., Brenninkmeijer, C. A. M., Frieß, U., Wagner, T., and Platt, U.: Airborne multi-axis DOAS measurements of atmospheric trace gases on CARIBIC long-distance flights, Atmos. Meas. Tech., 2, 639–652, https://doi.org/10.5194/amt-2-639-2009, 2009.

Dorf, M., Bösch, H., Butz, A., Camy-Peyret, C., Chipperfield, M. P., Engel, A., Goutail, F., Grunow, K., Hendrick, F., Hrechanyy, S., Naujokat, B., Pommereau, J.-P., Van Roozendael, M., Sioris, C., Stroh, F., Weidner, F., and Pfeilsticker, K.: Balloon-borne stratospheric BrO measurements: comparison with Envisat/SCIAMACHY BrO limb profiles, Atmos. Chem. Phys., 6, 2483–2501, https://doi.org/10.5194/acp-6-2483-2006, 2006.

Dorf, M., Butz, A., Camy-Peyret, C., Chipperfield, M. P., Kritten, L., and Pfeilsticker, K.: Bromine in the tropical troposphere and stratosphere as derived from balloon-borne BrO observations, Atmos. Chem. Phys., 8, 7265–7271, https://doi.org/10.5194/acp-8-7265-2008, 2008.

Drummond, J. W., Volz, A., and Ehhalt, D. H.: An optimized chemiluminescence detector for tropospheric NO measurements, J. Atmos. Chem., 2, 287–306, https://doi.org/10.1007/BF00051078, 1985.

Fahey, D., Eubank, C., Hübler, G., and Fehsenfeld, F.: Evaluation of a catalytic reduction technique for the measurement of total reactive odd-nitrogen NO_y in the atmosphere, J. Atmos. Chem., 3, 435–468, 1985.

Ferlemann, F., Bauer, N., Fitzenberger, R., Harder, H., Osterkamp, H., Perner, D., Platt, U., Scheider, M., Vradelis, P., and Pfeilsticker, K.: Differential optical absorption spectroscopy instrument for stratospheric balloon-borne trace gas studies, Appl. Optics, 39, 2377–2386, 2000.

Fitzenberger, R., Bösch, H., Camy-Peyret, C., Chpperfield, M., Harder, H., Platt, U., Pyle, J., Wagner, T., and Pfeilsticker, K.: First profile measurement of tropospheric BrO, Geophys. Res. Lett., 27, 2921–2924, 2000.

Fleischmann, O. C., Hartmann, M., Burrows, J. P., and Orphal, J.: New ultraviolet absorption cross-sections of BrO at atmospheric temperatures measured by time-windowing Fourier transform spectroscopy, J. Photoch. Photobio. A, 168, 117–132, 2004.

General, S., Pöhler, D., Sihler, H., Bobrowski, N., Frieß, U., Zielcke, J., Horbanski, M., Shepson, P. B., Stirm, B. H., Simpson, W. R., Weber, K., Fischer, C., and Platt, U.: The Heidelberg Airborne Imaging DOAS Instrument (HAIDI) – a novel imaging DOAS device for 2-D and 3-D imaging of trace gases and aerosols, Atmos. Meas. Tech., 7, 3459–3485, https://doi.org/10.5194/amt-7-3459-2014, 2014.

Gerilowski, K., Tretner, A., Krings, T., Buchwitz, M., Bertagnolio, P. P., Belemezov, F., Erzinger, J., Burrows, J. P., and Bovensmann, H.: MAMAP – a new spectrometer system for column-averaged methane and carbon dioxide observations from aircraft: instrument description and performance analysis, Atmos. Meas. Tech., 4, 215–243, https://doi.org/10.5194/amt-4-215-2011, 2011.

Gorshelev, V., Serdyuchenko, A., Weber, M., Chehade, W., and Burrows, J. P.: High spectral resolution ozone absorption cross-sections – Part 1: Measurements, data analysis and comparison with previous measurements around 293 K, Atmos. Meas. Tech., 7, 609–624, https://doi.org/10.5194/amt-7-609-2014, 2014.

Gratz, L. E., Ambrose, J. L., Jaffe, D. A., Shah, V., Jaeglé, L., Stutz, J., Festa, J., Spolaor, M., Tsai, C., Selin, N. E., Song, S., Zhou, X., Weinheimer, A. J., Knapp, D. J., Montzka, D. D., Flocke, F. M., Campos, T. L., Apel, E., Hornbrook, R., Blake, N. J., Hall, S., Tyndall, G. S., Reeves, M., Stechman, D., and Stell, M.: Oxidation of mercury by bromine in the subtropical Pacific free troposphere, Geophys. Res. Lett., 42, 10494–10502, https://doi.org/10.1002/2015GL066645, 2015.

Greenblatt, G. D., Orlando, J. J., Burkholder, J. B., and Ravishankara, A. R.: Absorption measurements of oxygen between 330 and 1140 nm, J. Geophys. Res., 95, 18577–18582, 1990.

Grooß, J.-U., Engel, I., Borrmann, S., Frey, W., Günther, G., Hoyle, C. R., Kivi, R., Luo, B. P., Molleker, S., Peter, T., Pitts, M. C., Schlager, H., Stiller, G., Vömel, H., Walker, K. A., and Müller, R.: Nitric acid trihydrate nucleation and denitrification in the Arctic stratosphere, Atmos. Chem. Phys., 14, 1055–1073, https://doi.org/10.5194/acp-14-1055-2014, 2014.

Großmann, K.: Aircraft-borne DOAS limb observations of UV/visible absorbing trace gas species over Borneo: Implications for the photochemistry of iodine, volatile organic oxide degradation, and lightning-produced radicals, PhD, University of Heidelberg, Heidelberg, Germany, https://doi.org/10.11588/heidok.00017874, 2014.

Gurlit, W., Bösch, H., Bovensmann, H., Burrows, J. P., Butz, A., Camy-Peyret, C., Dorf, M., Gerilowski, K., Lindner, A., Noël, S., Platt, U., Weidner, F., and Pfeilsticker, K.: The UV-A and visible solar irradiance spectrum: inter-comparison of absolutely calibrated, spectrally medium resolution solar irradiance spectra from balloon- and satellite-borne measurements, Atmos. Chem. Phys., 5, 1879–1890, https://doi.org/10.5194/acp-5-1879-2005, 2005.

Harder, H., Camy-Peyret, C., Ferlemann, F., Fitzenberger, R., Hawat, T., Osterkamp, H., Schneider, M., Perner, D., Platt, U., Vradelis, P., and Pfeilsticker, K.: Stratospheric BrO profiles measured at different latitudes and seasons: atmospheric observations, Geophys. Res. Lett., 25, 3843–3846, 1998.

Hendrick, F., Van Roozendael, M., Chipperfield, M. P., Dorf, M., Goutail, F., Yang, X., Fayt, C., Hermans, C., Pfeilsticker, K., Pommereau, J.-P., Pyle, J. A., Theys, N., and De Mazière, M.: Retrieval of stratospheric and tropospheric BrO profiles and columns using ground-based zenith-sky DOAS observations at Harestua, 60° N, Atmos. Chem. Phys., 7, 4869–4885, https://doi.org/10.5194/acp-7-4869-2007, 2007.

Heue, K.-P., Wagner, T., Broccardo, S. P., Walter, D., Piketh, S. J., Ross, K. E., Beirle, S., and Platt, U.: Direct observation of two dimensional trace gas distributions with an airborne Imaging DOAS instrument, Atmos. Chem. Phys., 8, 6707–6717, https://doi.org/10.5194/acp-8-6707-2008, 2008.

Heue, K.-P., Riede, H., Walter, D., Brenninkmeijer, C. A. M., Wagner, T., Frieß, U., Platt, U., Zahn, A., Stratmann, G., and Ziereis, H.: CARIBIC DOAS observations of nitrous acid and formaldehyde in a large convective cloud, Atmos. Chem. Phys., 14, 6621–6642, https://doi.org/10.5194/acp-14-6621-2014, 2014.

Hüneke, T.: The scaling method applied to HALO measurements: Inferring absolute trace gas concentrations from airborne limb spectroscopy under all sky conditions, PhD, University of Heidelberg, Heidelberg, Germany, available at: http://www.ub.uni-heidelberg.de/archiv/22573 (last access: 30 October 2017), 2016.

Jöckel, P., Kerkweg, A., Pozzer, A., Sander, R., Tost, H., Riede, H., Baumgaertner, A., Gromov, S., and Kern, B.: Development cycle 2 of the Modular Earth Submodel System (MESSy2), Geosci. Model Dev., 3, 717–752, https://doi.org/10.5194/gmd-3-717-2010, 2010.

Jöckel, P., Tost, H., Pozzer, A., Kunze, M., Kirner, O., Brenninkmeijer, C. A. M., Brinkop, S., Cai, D. S., Dyroff, C., Eckstein, J., Frank, F., Garny, H., Gottschaldt, K.-D., Graf, P., Grewe, V., Kerkweg, A., Kern, B., Matthes, S., Mertens, M., Meul, S., Neumaier, M., Nützel, M., Oberländer-Hayn, S., Ruhnke, R., Runde, T., Sander, R., Scharffe, D., and Zahn, A.: Earth System Chemistry integrated Modelling (ESCiMo) with the Modular Earth Submodel System (MESSy) version 2.51, Geosci. Model Dev., 9, 1153–1200, https://doi.org/10.5194/gmd-9-1153-2016, 2016.

Jurkat, T., Voigt, C., Kaufmann, S., Zahn, A., Sprenger, M., Hoor, P., Bozem, H., Müller, S., Dörnbrack, A., Schlager, H., Bönisch, H., and Engel, A.: A quantitative analysis of stratospheric HCl, HNO_3, and O_3 in the tropopause region near the subtropical jet, Geophys. Res. Lett., 41, 3315–3321, https://doi.org/10.1002/2013GL059159, 2014.

Jurkat, T., Voigt, C., Kaufmann, S., Grooß, J.-U., Ziereis, H., Dörnbrack, A., Hoor, P., Bozem, H., Engel, A., Bönisch, H., Keber, T., Hüneke, T., Pfeilsticker, K., Zahn, A., Walker, K. A., Boone, C. D., Bernath, P. F., and Schlager, H.: Depletion of ozone and reservoir species of chlorine and nitrogen oxide in the lower Antarctic polar vortex measured from aircraft, Geophys. Res. Lett., 44, 6440–6449, https://doi.org/10.1002/2017GL073270, 2017.

Klepp, C., Ament, F., Bakan, S., Hirsch, L., and Stevens, B.: The NARVAL Campaign Report, Max Planck Institute for Meteorology, Hamburg, Germany, 2014.

Knecht, M.: Simulation of radiative field modification due to tropical clouds, Master's thesis, Institut für Umweltphysik, Universität of Heidelberg, Heidelberg, Germany, available at: http://www.iup.uni-heidelberg.de/institut/forschung/groups/atmosphere/stratosphere/publications/pdf/MA_thesis_Matthias_final.pdf (last access: 30 October 2017), 2015.

Kreycy, S., Camy-Peyret, C., Chipperfield, M. P., Dorf, M., Feng, W., Hossaini, R., Kritten, L., Werner, B., and Pfeilsticker, K.: Atmospheric test of the $J(BrONO_2) / k_{BrO+NO_2}$ ratio: implications for total stratospheric Bry and bromine-mediated ozone loss, Atmos. Chem. Phys., 13, 6263–6274, https://doi.org/10.5194/acp-13-6263-2013, 2013.

Kritten, L., Butz, A., Dorf, M., Deutschmann, T., Kühl, S., Prados-Roman, C., Pukite, J., Rozanov, A., Schofield, R., and Pfeilsticker, K.: Time dependent profile retrieval of UV/vis absorbing radicals from balloon-borne limb measurements – a case study on NO_2 and O_3, Atmos. Meas. Tech., 3, 933–946, https://doi.org/10.5194/amt-3-933-2010, 2010.

Kritten, L., Butz, A., Chipperfield, M. P., Dorf, M., Dhomse, S., Hossaini, R., Oelhaf, H., Prados-Roman, C., Wetzel, G., and Pfeilsticker, K.: Constraining the N_2O_5 UV absorption cross section from spectroscopic trace gas measurements in the tropical mid-stratosphere, Atmos. Chem. Phys., 14, 9555–9566, https://doi.org/10.5194/acp-14-9555-2014, 2014.

Kromminga, H., Orphal, J., Spietz, P., Voigt, S., and Burrows, J.: New measurements of OClO absorption cross-sections in the 325–435 nm region and their temperature dependence between 213 and 293 K, J. Photoch. Photobio. A, 157, 149–160, 2003.

McElroy, C. T., McLinden, C. A., and McConnell, J. C.: Evidence for bromine monoxide in the free troposphere during the Arctic polar sunrises, Nature, 397, 338–341, 1999.

Merlaud, A., Van Roozendael, M., van Gent, J., Fayt, C., Maes, J., Toledo-Fuentes, X., Ronveaux, O., and De Mazière, M.: DOAS measurements of NO_2 from an ultralight aircraft during the Earth Challenge expedition, Atmos. Meas. Tech., 5, 2057–2068, https://doi.org/10.5194/amt-5-2057-2012, 2012.

Müller, S., Hoor, P., Bozem, H., Gute, E., Vogel, B., Zahn, A., Bönisch, H., Keber, T., Krämer, M., Rolf, C., Riese, M., Schlager, H., and Engel, A.: Impact of the Asian monsoon on the extratropical lower stratosphere: trace gas observations during TACTS over Europe 2012, Atmos. Chem. Phys., 16, 10573–10589, https://doi.org/10.5194/acp-16-10573-2016, 2016.

Noxon, J. F.: Nitrogen dioxide in the stratosphere and troposphere measured by ground-based absorption spectroscopy, Science, 189, 547–549, https://doi.org/10.1126/science.189.4202.547, 1975.

Noxon, J. F., Whipple, E. C., and Hyde, R. S.: Stratospheric NO_2: 1. Observational method and behavior at mid-latitude, J. Geophys. Res.-Oceans, 84, 5047–5065, https://doi.org/10.1029/JC084iC08p05047, 1979.

Oikarinen, L.: Effect of surface albedo variations on UV-visible limb-scattering measurements of the atmosphere, J. Geophys. Res.-Atmos., 107, ACH 13-1–ACH 13-15, https://doi.org/10.1029/2001JD001492, 2002.

Pfeilsticker, K. and Platt, U.: Airborne measurements during the Arctic Stratospheric Experiment: Observation of O_3 and NO_2, Geophys. Res. Lett., 21, 1375–1378, https://doi.org/10.1029/93GL01870, 1994.

Pfeilsticker, K., Bösch, H., Camy-Peyret, C., Fitzenberger, R., Harder, H., and Osterkamp, H.: First atmospheric profile measurements of the atmospheric UV/vis O_4 absorption bands strength: Implications for the spectroscopy and the formation enthalpy of the O_2–O_2 dimer, Geophys. Res. Lett., 28, 4595–4598, https://doi.org/10.1029/2001GL013734, 2001.

Platt, U. and Stutz, J.: Differential Optical Absorption Spectroscopy (DOAS), Principle and Applications, Springer Verlag, Heidelberg, 2008.

Prados-Roman, C., Butz, A., Deutschmann, T., Dorf, M., Kritten, L., Minikin, A., Platt, U., Schlager, H., Sihler, H., Theys, N., Van Roozendael, M., Wagner, T., and Pfeilsticker, K.: Airborne DOAS limb measurements of tropospheric trace gas profiles: case studies on the profile retrieval of O_4 and BrO, Atmos. Meas. Tech., 4, 1241–1260, https://doi.org/10.5194/amt-4-1241-2011, 2011.

Raecke, R.: Atmospheric spectoscopy of trace gases and water vapour in the tropical tropopause layer from the NASA Global Hawk, Master thesis, Institut für Umweltphysik, Universität Heidelberg, available at: http://www.iup.uni-heidelberg.de/institut/forschung/groups/atmosphere/stratosphere/publications/pdf/MScThesis_Rasmus_Raecke.pdf (last access: 30 October 2017), 2013.

Rodgers, C.: Inverse methods for atmospheric sounding, World Scientific, Singapore, New Jersey, London, Hongkong, 2000.

Roeckner, E., Brokopf, R., Esch, M., Giorgetta, M., Hagemann, S., Kornblueh, L., Manzini, E., Schlese, U., and Schulzweida, U.: Sensitivity of Simulated Climate to Horizontal and Vertical Resolution in the ECHAM5 Atmosphere Model, J. Climate, 19, 3771–3791, https://doi.org/10.1175/JCLI3824.1, 2006.

Rolf, C., Afchine, A., Bozem, H., Buchholz, B., Ebert, V., Guggenmoser, T., Hoor, P., Konopka, P., Kretschmer, E., Müller, S., Schlager, H., Spelten, N., Suminska-Ebersoldt, O., Ungermann, J., Zahn, A., and Krämer, M.: Transport of Antarctic stratospheric strongly dehydrated air into the troposphere observed during the HALO-ESMVal campaign 2012, Atmos. Chem. Phys., 15, 9143–9158, https://doi.org/10.5194/acp-15-9143-2015, 2015.

Rothman, L. S., Gordon, I. E., Barbe, A., Benner, D. C., Bernath, P. F., Birk, M., Boudon, V., Brown, L. R., Campargue, A., Champion, J.-P., Tashkun, S. A., Tennyson, J., Toth, R. A., Vandaele, A. C., and Vander Auwera, J.: The HITRAN 2008 molecular spectroscopic database, J. Quant. Spectrosc. Ra., 110, 533–572, 2009.

Saiz-Lopez, A. and von Glasow, R.: Reactive halogen chemistry in the troposphere, Chem. Soc. Rev., 41, 6448–6472, 2012.

Sander, R., Baumgaertner, A., Gromov, S., Harder, H., Jöckel, P., Kerkweg, A., Kubistin, D., Regelin, E., Riede, H., Sandu, A., Taraborrelli, D., Tost, H., and Xie, Z.-Q.: The atmospheric chemistry box model CAABA/MECCA-3.0, Geosci. Model Dev., 4, 373–380, https://doi.org/10.5194/gmd-4-373-2011, 2011a.

Sander, S. P., Abbatt, J., Barker, J. R., Burkholder, J. B., Friedl, R. R., Golden, D. M., Huie, R. E., Kolb, C. E., Kurylom, M. J., Moortgat, G. K., Orkin, V. L., and Wine, P. H.: Chemical Kinetics and Photochemical Data for Use in Atmospheric Studies, Evaluation No. 17, JPL Publication 10-6, Jet Propulsion Laboratory, Pasadena, available at: http://jpldataeval.jpl.nasa.gov (last access: 30 October 2017), 2011b.

Scalone, L.: Retrieval of Cirrus Optical Properties in the near-IR spectral range within the NASA ATTREX Project, PhD, University of Heidelberg, Heidelberg, Germany, https://doi.org/10.11588/heidok.00023004, 2017.

Schiller, C., Wahner, A., Platt, U., Dorn, H.-P., Callies, J., and Ehhalt, D. H.: Near UV atmospheric absorption measurements of column abundances during Airborne Arctic Stratospheric Expedition, January–February 1989: 2. OClO observations, Geophys. Res. Lett., 17, 501–504, https://doi.org/10.1029/GL017i004p00501, 1990.

Schiller, C., Bozem, H., Gurk, C., Parchatka, U., Königstedt, R., Harris, G., Lelieveld, J., and Fischer, H.: Applications of quantum cascade lasers for sensitive trace gas measurements of CO, CH_4, N_2O and HCHO, Appl. Phys. B, 92, 419–430, https://doi.org/10.1007/s00340-008-3125-0, 2008.

Schmidt, J. A., Jacob, D. J., Horowitz, H. M., Hu, L., Sherwen, T., Evans, M. J., Liang, Q., Suleiman, R. M., Oram, D. E., Le Breton, M., Percival, C. J., Wang, S., Dix, B., and Volkamer, R.: Modeling the observed tropospheric BrO background: Importance of multiphase chemistry and implications for ozone, OH, and mercury, J. Geophys. Res.-Atmos., 121, 11819–11835, https://doi.org/10.1002/2015JD024229, 2016.

Serdyuchenko, A., Gorshelev, V., Weber, M., Chehade, W., and Burrows, J. P.: High spectral resolution ozone absorption cross-sections – Part 2: Temperature dependence, Atmos. Meas. Tech., 7, 625–636, https://doi.org/10.5194/amt-7-625-2014, 2014.

Sherwen, T., Schmidt, J. A., Evans, M. J., Carpenter, L. J., Großmann, K., Eastham, S. D., Jacob, D. J., Dix, B., Koenig, T. K., Sinreich, R., Ortega, I., Volkamer, R., Saiz-Lopez, A., Prados-Roman, C., Mahajan, A. S., and Ordóñez, C.: Global impacts of tropospheric halogens (Cl, Br, I) on oxidants and composition in GEOS-Chem, Atmos. Chem. Phys., 16, 12239–12271, https://doi.org/10.5194/acp-16-12239-2016, 2016.

Sherwen, T., Evans, M. J., Carpenter, L. J., Schmidt, J. A., and Mickley, L. J.: Halogen chemistry reduces tropospheric O_3 radiative forcing, Atmos. Chem. Phys., 17, 1557–1569, https://doi.org/10.5194/acp-17-1557-2017, 2017.

Solomon, S., Mount, G. H., Sanders, R. W., and Schmeltekopf, A. L.: Visible spectroscopy at McMurdo Station, Antarctica: 2. Observations of OClO, J. Geophys. Res.-Atmos., 92, 8329–8338, https://doi.org/10.1029/JD092iD07p08329, 1987a.

Solomon, S., Schmeltekopf, A. L., and Sanders, R. W.: On the interpretation of zenith sky absorption measurements, J. Geophys. Res.-Atmos., 92, 8311–8319, https://doi.org/10.1029/JD092iD07p08311, 1987b.

Stratmann, G., Ziereis, H., Stock, P., Brenninkmeijer, C., Zahn, A., Rauthe-Schöch, A., Velthoven, P., Schlager, H., and Volz-Thomas, A.: NO and NO_y in the upper troposphere: Nine years of CARIBIC measurements onboard a passenger aircraft, Atmos. Environ., 133, 93–111, https://doi.org/10.1016/j.atmosenv.2016.02.035, 2016.

Stutz, J., Kim, E., Platt, U., Bruno, P., Perrino, C., and Febo, A.: UV-visible absorption cross sections of nitrous acid, J. Geophys. Res.-Atmos., 105, 14585–14592, https://doi.org/10.1029/2000JD900003, 2000.

Stutz, J., Werner, B., Spolaor, M., Scalone, L., Festa, J., Tsai, C., Cheung, R., Colosimo, S. F., Tricoli, U., Raecke, R., Hossaini, R., Chipperfield, M. P., Feng, W., Gao, R.-S., Hintsa, E. J., Elkins, J. W., Moore, F. L., Daube, B., Pittman, J., Wofsy, S., and Pfeilsticker, K.: A new Differential Optical Absorption Spectroscopy instrument to study atmospheric chemistry from a high-

altitude unmanned aircraft, Atmos. Meas. Tech., 10, 1017–1042, https://doi.org/10.5194/amt-10-1017-2017, 2017.

Thalman, R. and Volkamer, R.: Temperature dependent absorption cross-sections of O_2-O_2 collision pairs between 340 and 630 nm and at atmospherically relevant pressure, Phys. Chem. Chem. Phys., 15, 15371–15381, https://doi.org/10.1039/C3CP50968K, 2013.

Van Roozendael, M., Wagner, T., Richter, A., Pundt, I., Arlander, D., Burrows, J., Chipperfield, M. P., Fayt, C., Johnston, P., Lambert, J., Kreher, K., Pfeilsticker, K., Platt, U., Pommereau, J. P., Sinnhuber, B., Tornkvist, K., and Wittrock, F.: Intercomparison of BrO Measurements from ERS-2 GOME, Ground-based and balloon platforms, Adv. Space Res., 29, 1161–1666, 2002.

Vogel, B., Günther, G., Müller, R., Grooß, J.-U., Hoor, P., Krämer, M., Müller, S., Zahn, A., and Riese, M.: Fast transport from Southeast Asia boundary layer sources to northern Europe: rapid uplift in typhoons and eastward eddy shedding of the Asian monsoon anticyclone, Atmos. Chem. Phys., 14, 12745–12762, https://doi.org/10.5194/acp-14-12745-2014, 2014.

Vogel, B., Günther, G., Müller, R., Grooß, J.-U., and Riese, M.: Impact of different Asian source regions on the composition of the Asian monsoon anticyclone and of the extratropical lowermost stratosphere, Atmos. Chem. Phys., 15, 13699–13716, https://doi.org/10.5194/acp-15-13699-2015, 2015.

Voigt, C., Schumann, U., Minikin, A., Abdelmonem, A., Afchine, A., Borrmann, S., Boettcher, M., Buchholz, B., Bugliaro, L., Costa, A., Curtius, J., Dollner, M., Dörnbrack, A., Dreiling, V., Ebert, V., Ehrlich, A., Fix, A., Forster, L., Frank, F., Fütterer, D., Giez, A., Graf, K., Grooß, J.-U., Groß, S., Heimerl, K., Heinold, B., Hüneke, T., Järvinen, E., Jurkat, T., Kaufmann, S., Kenntner, M., Klingebiel, M., Klimach, T., Kohl, R., Krämer, M., Krisna, T. C., Luebke, A., Mayer, B., Mertes, S., Molleker, S., Petzold, A., Pfeilsticker, K., Port, M., Rapp, M., Reutter, P., Rolf, C., Rose, D., Sauer, D., Schäfler, A., Schlage, R., Schnaiter, M., Schneider, J., Spelten, N., Spichtinger, P., Stock, P., Walser, A., Weigel, R., Weinzierl, B., Wendisch, M., Werner, F., Wernli, H., Wirth, M., Zahn, A., Ziereis, H., and Zöger, M.: ML-CIRRUS – The airborne experiment on natural cirrus and contrail cirrus with the high-altitude long-range research aircraft HALO, B. Am. Meteorol. Soc., 98, 271–288, https://doi.org/10.1175/BAMS-D-15-00213.1, 2017.

Volkamer, R., Baidar, S., Campos, T. L., Coburn, S., DiGangi, J. P., Dix, B., Eloranta, E. W., Koenig, T. K., Morley, B., Ortega, I., Pierce, B. R., Reeves, M., Sinreich, R., Wang, S., Zondlo, M. A., and Romashkin, P. A.: Aircraft measurements of BrO, IO, glyoxal, NO_2, H_2O, O_2–O_2 and aerosol extinction profiles in the tropics: comparison with aircraft-/ship-based in situ and lidar measurements, Atmos. Meas. Tech., 8, 2121–2148, https://doi.org/10.5194/amt-8-2121-2015, 2015.

von Glasow, R., von Kuhlmann, R., Lawrence, M. G., Platt, U., and Crutzen, P. J.: Impact of reactive bromine chemistry in the troposphere, Atmos. Chem. Phys., 4, 2481–2497, https://doi.org/10.5194/acp-4-2481-2004, 2004.

Wagner, T., Beirle, S., and Deutschmann, T.: Three-dimensional simulation of the Ring effect in observations of scattered sun light using Monte Carlo radiative transfer models, Atmos. Meas. Tech., 2, 113–124, https://doi.org/10.5194/amt-2-113-2009, 2009.

Wahner, A., Callies, J., Dorn, H.-P., Platt, U., and Schiller, C.: Near UV atmospheric absorption measurements of column abundances during Airborne Arctic Stratospheric Expedition, January–February 1989: 1. Technique and NO2 observations, Geophys. Res. Lett., 17, 497–500, https://doi.org/10.1029/GL017i004p00497, 1990a.

Wahner, A., Callies, J., Dorn, H.-P., Platt, U., and Schiller, C.: Near UV atmospheric absorption measurements of column abundances during Airborne Arctic Stratospheric Expedition, January–February 1989: 3. BrO observations, Geophys. Res. Lett., 17, 517–520, https://doi.org/10.1029/GL017i004p00517, 1990b.

Wang, S., Schmidt, J. A., Baidar, S., Coburn, S., Dix, B., Koenig, T. K., Apel, E., Bowdalo, D., Campos, T. L., Eloranta, E., Evans, M. J., DiGangi, J. P., Zondlo, M. A., Gao, R.-S., Haggerty, J. A., Hall, S. R., Hornbrook, R. S., Jacob, D., Morley, B., Pierce, B., Reeves, M., Romashkin, P., ter Schure, A., and Volkamer, R.: Active and widespread halogen chemistry in the tropical and subtropical free troposphere, P. Natl. Acad. Sci. USA, 112, 9281–9286, https://doi.org/10.1073/pnas.1505142112, 2015.

Weidner, F., Bösch, H., Bovensmann, H., Burrows, J. P., Butz, A., Camy-Peyret, C., Dorf, M., Gerilowski, K., Gurlit, W., Platt, U., von Friedeburg, C., Wagner, T., and Pfeilsticker, K.: Balloon-borne limb profiling of UV/vis skylight radiances, O_3, NO_2, and BrO: technical set-up and validation of the method, Atmos. Chem. Phys., 5, 1409–1422, https://doi.org/10.5194/acp-5-1409-2005, 2005.

Wendisch, M., Pöschl, U., Andreae, M. O., Machado, L. A. T., Albrecht, R., Schlager, H., Rosenfeld, D., Martin, S. T., Abdelmonem, A., Afchine, A., Araùjo, A., Artaxo, P., Aufmhoff, H., Barbosa, H. M. J., Borrmann, S., Braga, R., Buchholz, B., Cecchini, M. A., Costa, A., Curtius, J., Dollner, M., Dorf, M., Dreiling, V., Ebert, V., Ehrlich, A., Ewald, F., Fisch, G., Fix, A., Frank, F., Fütterer, D., Heckl, C., Heidelberg, F., Hüneke, T., Jäkel, E., Järvinen, E., Jurkat, T., Kanter, S., Kästner, U., Kenntner, M., Kesselmeier, J., Klimach, T., Knecht, M., Kohl, R., Kölling, T., Krämer, M., Krüger, M., Krisna, T. C., Lavric, J. V., Longo, K., Mahnke, C., Manzi, A. O., Mayer, B., Mertes, S., Minikin, A., Molleker, S., Münch, S., Nillius, B., Pfeilsticker, K., Pöhlker, C., Roiger, A., Rose, D., Rosenow, D., Sauer, D., Schnaiter, M., Schneider, J., Schulz, C., de Souza, R. A. F., Spanu, A., Stock, P., Vila, D., Voigt, C., Walser, A., Walter, D., Weigel, R., Weinzierl, B., Werner, F., Yamasoe, M. A., Ziereis, H., Zinner, T., and Zöger, M.: The ACRIDICON-CHUVA campaign: Studying tropical deep convective clouds and precipitation over Amazonia using the new German research aircraft HALO, B. Am. Meteorol. Soc., 97, 1885–1908, https://doi.org/10.1175/BAMS-D-14-00255.1, 2016.

Werner, B.: Spectroscopic UV/vis limb measurements from aboard the NASA Global Hawk: Implications for the photochemistry and budget of bromine in the tropical tropopause layer, PhD, University of Heidelberg, Heidelberg, Germany, 2015.

Werner, B., Stutz, J., Spolaor, M., Scalone, L., Raecke, R., Festa, J., Colosimo, S. F., Cheung, R., Tsai, C., Hossaini, R., Chipperfield, M. P., Taverna, G. S., Feng, W., Elkins, J. W., Fahey, D. W., Gao, R.-S., Hintsa, E. J., Thornberry, T. D., Moore, F. L., Navarro, M. A., Atlas, E., Daube, B. C., Pittman, J., Wofsy, S., and Pfeilsticker, K.: Probing the subtropical lowermost stratosphere and the tropical upper troposphere and tropopause layer

for inorganic bromine, Atmos. Chem. Phys., 17, 1161–1186, https://doi.org/10.5194/acp-17-1161-2017, 2017.

Wolf, K., Ehrlich, A., Hüneke, T., Pfeilsticker, K., Werner, F., Wirth, M., and Wendisch, M.: Potential of remote sensing of cirrus optical thickness by airborne spectral radiance measurements at different sideward viewing angles, Atmos. Chem. Phys., 17, 4283–4303, https://doi.org/10.5194/acp-17-4283-2017, 2017.

Ye, C., Zhou, X., Pu, D., Stutz Jochen, Festa, J., Spolaor, M., Tsai, C., Cantrell, C., Mauldin, R. L., Campos, T., Weinheimer, A., Hornbrook, R. S., Apel, E. C., Guenther, A., Kaser, L., Yuan, B., Karl, T., Haggerty, J., Hall, S., Ullmann, K., Smith, J. N., Ortega, J., and Knote, C.: Rapid cycling of reactive nitrogen in the marine boundary layer, Nature, 532, 489–491, https://doi.org/10.1038/nature17195, 2016.

Zahn, A., Weppner, J., Widmann, H., Schlote-Holubek, K., Burger, B., Kühner, T., and Franke, H.: A fast and precise chemiluminescence ozone detector for eddy flux and airborne application, Atmos. Meas. Tech., 5, 363–375, https://doi.org/10.5194/amt-5-363-2012, 2012.

Ziereis, H., Schlager, H., Schulte, P., Velthoven, P. v., and Slemr, F.: Distributions of NO, NO_x, and NO_y in the upper troposphere and lower stratosphere between 28 and 61 N during POLINAT 2, J. Geophys. Res.-Atmos., 105, 3653–3664, 2000.